Compliance method to measure crack length and crack closure for automated fatigue crack propagation test of nanocrystalline nickel film

Nakai, Yoshikazu
Hirai, Tsuyoshi
Kikuchi, Shoichi

(Citation)
Engineering Fracture Mechanics,254:107925

(Issue Date)
2021-09

(Resource Type)
journal article

(Version)
Accepted Manuscript

Compliance Method to Measure Crack Length and Crack Closure for Automated Fatigue Crack Propagation Test of Nanocrystalline Nickel Film

Yoshikazu Nakai
Department of Mechanical Engineering, Kobe University, Nada, Kobe 657-8501, Japan
nakai@mech.kobe-u.ac.jp
Corresponding author

Tsuyoshi Hirai
Department of Mechanical Engineering, Kobe University, Nada, Kobe 657-8501, Japan
ht244s14go@gmail.com

Shoichi Kikuchi
Department of Mechanical Engineering, Shizuoka University, Naka, Hamamatsu 432-8561, Japan
kikuchi.shoichi@shizuoka.ac.jp

Key words: Crack closure; Crack growth rate; Experimental technique; Grain size; Threshold stress intensity factor

Nomenclature

a: Crack length

$a_{act,fin}$: Final crack length measured by optical microscopy

$a_{act,ini}$: Initial crack length measured by optical microscopy

$a_{cal,fin}$: Calculated final crack length

$a_{cal,ini}$: Calculated initial crack length

B: Specimen thickness

C: Compliance

da/dN: Crack propagation rate

E: Young's modulus

k: Force shedding rate

$K_{max,th}$: Maximum stress intensity factor under the threshold condition

$K_{min,th}$: Minimum stress intensity factor under the threshold condition

$K_{op,th}$: Crack opening stress intensity factor under the threshold condition

L: Gauge length (distance between grips)

P: Applied force

P_{max} : Maximum applied force

P_{min}: Minimum applied forces

R: Force ratio = P_{min}/P_{max}

V: Loading point displacement

W: Specimen width

Δa: Crack extension

ΔK: Stress intensity factor range

ΔK_{eff}: Effective stress intensity factor range

ΔK_{th}: Stress intensity factor range under the threshold condition

ε_b: Back face strain

Abstract

Experimental techniques for measuring the crack length and crack closure behavior of single edge crack tension [SE(T)] specimens with fixed ends were developed with compliance method employing a high-resolution laser displacement meter together with data processing for noise elimination. Then, an automatic force-shedding fatigue crack propagation test system was developed. Using this system, we measured the crack length and crack closure behavior of thin films with a thickness of 5 or 10 μm and width of 10 mm, with which the accuracy of crack length measurement was better than 0.46 mm. The crack closure behavior could also be identified by the compliance method. The relationship between the crack propagation rate da/dN and the stress intensity factor range ΔK for nanocrystalline (NC) and ultrafine-grained (UFG) thin film was independent of the force ratio, and the relationship for the 10 μm-thick film was almost identical to that for the 5 μm thick film. No crack closure was observed in the UFG and NC thin films, whereas it occurred in the medium-size-grained (MG) thin film. The da/dN–ΔK_{eff} relationships for thin films were independent of the force ratio and film thickness. In the Paris law region, da/dN for the MG film was higher than that for an MG plate at comparable ΔK_{eff}, showing that crack closure could not account for the thickness effect. However, no difference in $\Delta K_{\mathrm{eff,th}}$ was observed for both the MG film and the MG plate. In the Paris law region (Region B), no effect of grain size on the da/dN–ΔK relationship was observed for the 10-μm-thick film; however, the crack propagation rate was higher for a film with smaller grain size and thickness from 100 to 180 μm. For NC and UFG films, the crack propagation rate of the 100-μm-thick film was higher than that of the 10-μm-thick film, but it was almost identical for MG films; however, the rate for a thin film was higher than that for a bulk plate. The threshold stress intensity factor range was always lower for a film with smaller grain size.

1. Introduction

The nanocrystallization of metals and alloys is one of the most promising techniques for improving their strength [1–5] and resistance to wear because grain refinement usually leads to an increase in strength [6, 7], and their thin films are now being widely used for micro-electro-mechanical systems. The electrodeposition method will be the easiest method of obtaining a uniform nanocrystalline structure in thin films [8, 9]. Before nanocrystalline thin films can be widely used in engineering applications, their damage tolerance should be guaranteed, especially their fatigue crack propagation resistance.

It is well known from fracture mechanics studies of conventional bulk metals and alloys that the fatigue crack propagation resistance usually decreases with grain refinement and an increase in force ratio [10], especially in the region near the threshold. These effects have been explained by the crack closure mechanism. The threshold stress intensity factor range is one of the most important

fatigue properties in damage tolerance design, and its determination requires the ΔK-shedding test employing computer-aided automated crack length measurement, which is designated by ASTM as E647-15 for bulk materials.

In the study of fatigue crack propagation, an automated crack length measurement system is required to reduce experimental cost, obtain high accuracy [l1], and facilitate testing under stress-intensity-factor (K) control. Techniques, such as the compliance, electrical potential drop, acoustic emission, and ultrasonic methods, have been used for the measurement of long cracks [12]. Of these, the compliance and electrical potential drop method are considered to be superior for the quantitative measurement of crack length and suitable for the automated fatigue crack propagation test because the measured values can be easily converted to digital values without the needs for complicated procedures. The electrical potential drop method may be the simplest technique for crack length measurement in which both direct current (DC) and alternating current (AC) may be used. The DC method is more commonly used because the apparatus is simple, and analytical calibration relationships may be more readily obtained. The DC methods are somewhat limited, however, because of their sensitivity to thermally induced electromotive force or potential associated with the thermocouple effect at junctions of dissimilar metals. Moreover, high current is needed to achieve the desired sensitivity. AC systems utilize a lock-in amplifier with excellent noise elimination capabilities to measure electrical potential drop [13–16]. Because of the high signal-to-noise capability of the lock-in amplifier and its operation as a tuned amplifier, the AC systems can be operated at lower current levels than equivalent DC systems and are insensitive to the thermally induced DC electromotive force [13–16]. However, the crack closure behavior cannot be monitored by the electrical potential drop method because it is difficult to separate the effects of crack closure from those of crack tip plasticity, and electromagnetic induction between crack faces which occurring in AC systems [16].

Compliance methods have been widely used for measuring the crack length and crack closure. These methods are based on the measurement of the crack opening displacement or strain. For bending-type specimens such as compact [C(T)] and four-point bending specimens, the change in far-field compliance with crack extension is large enough to measure the crack length and crack closure. Nakabo et al. successfully measured the crack length for four-point bending specimens by measuring the compliance with piston displacement [17]. However, these methods employ the compliance evaluated near the crack for axial-loading-type specimens such as middle tension (MT(T)) [10] and single edge crack tension (SE(T)) specimens because the change in far-field compliance with crack extension is extremely small. Shape and Su developed a technique using a laser-based interferometric strain/displace gauge [18], and this technique was applied to crack closure measurement of an axial-loading-type bulk specimen [18–20]. However, it cannot be applied to thin

films because it requires two closely spaced indentations pressed into the surface of a specimen with a Vickers microhardness tester.

Since compressive stress is generated within bending-type specimens and causes buckling of a thin film, SE(T) specimens have usually been employed in the fatigue crack propagation test of thin films; however, it is impossible to install a displacement or strain gauge on the specimen near the crack without causing a serious change in the stiffness of the specimen. Grünewald et al. successfully measured crack lengths of micro specimens by the compliance method using the nanoindentation module of a scanning electron microscope. In their experiments, no crack closure behavior was observed [21].

Visual methods, such as optical microscopy, are the most conventional methods for crack length measurement [22–26], and scanning electron microscopy is also employed for the measurement in fatigue crack propagation tests. Recently, the visual method aided by the digital image correlation (DIC) is developed for crack length measurements [27]. Crack closure is also measured by the DIC method [26–28]. However, these visual methods are not suitable for in situ automated fatigue crack length measurements because of the long processing time that makes the fatigue crack propagation test cumbersome.

In a review of the propagation of short fatigue cracks, Suresh and Ritchie pointed out that the application of fracture mechanics to the propagation of fatigue cracks implicitly indicates that the concept of similitude is valid and that the governing parameter, such as the stress intensity factor K or the J -integral, used to correlate crack propagation rates fully describes the stress and deformation fields in the vicinity of the crack tip [29]. This similitude concept implies that, for two cracks of different sizes subjected to the same stress intensity factor (under small-scale yielding) in a given material–microstructure–environment system, crack tip plastic zones are equal in size and the stress and strain distributions along the borders of these zones (ahead of the crack) are identical. This 'lack of similitude' problem arises for a number of reasons including the existence of (i) local microstructural features that do not substantially alter the propagation of large cracks but can interact strongly with small cracks because they are of comparable size (microstructurally short cracks) [30–33], (ii) differences in the crack closure behavior (physically/mechanically short cracks) [34–42], and (iii) differences in the local crack tip environments (chemically short cracks) [43–51]. In testing of bulk materials in an inert environment, the crack closure effect is the most influential factor underlying the breakdown of the similitude concept, whereas the microstructural effect appears only for very short cracks. For a low-dimensional specimen, which is employed for micro-electro-mechanical systems, made of conventional materials, however, the microstructural effect should be considered in the application of fracture mechanics to fatigue crack propagation [21], where the low-dimensional specimen is defined as having at least one size of specimen is small compared with the

bulk specimen. Nanocrystalline materials can mitigate the breakdown of the similitude concept owing to the microstructural effect and expand the application of fracture mechanics to fatigue crack propagation. In addition, the nanocrystallization of microsamples can be expected to strengthen micro-electro-mechanical systems.

On the other hand, Kondo et al. [52] reported that fatigue damage in submicron-thickness copper films differs from that in bulk materials. Then, the study of fatigue crack propagation on a thin film, which is a low-dimensional material, brings about another factor that can affect the breakdown of the similitude concept regardless of crack length, whereas most of the previous studies on electrodeposited nickel films were focused on the effect of nanocrystallinity. Unfortunately, the thickness effect has not been considered, and sheets thicker than 100 μm have been employed for the study of fatigue crack propagation in nanocrystalline metals.

The effect of grain size on the fatigue crack propagation rate in the Paris law region (Region B) of an electrodeposited nanocrystalline nickel sheet was studied by Hanlon et al.[23] and Cavaliere [26] under a constant imposed cyclic force range, and they found that the rate was higher for a smaller grain size. Sangid et al. measured the crack closure of a nanocrystalline sheet, wherein the crack opening displacement was measured as a function of the distance from the crack tip at five force levels [27], although ASTM E647-15 suggests that each segment span for calculating compliance offset should be 10 % of the cyclic force range. This means that more than twenty sampling points are required for unloading half a cycle because more than two sampling points are necessary to calculate compliance in each segment span. To determine the fatigue crack mechanism, Xie et al. measured the striation spacing and associated shear band width, and found that both increased with crack length in the Paris law region [24]. This result was obtained by a constant-applied-force range fatigue test; as a result, the crack propagation rate was found to be higher than 10^{-9} m/cycle (Region B). Tanaka et al. conducted the force shedding fatigue crack propagation test of a nanocrystalline nickel thin film with a thickness of 10 μm to examine the effect of grain size on the threshold condition. The crack length was optically monitored under a digital microscope and force shedding was conducted manually [25].

In the present study, an automated fatigue crack propagation test system, which enabled the force shedding fatigue crack propagation test for a self-standing SE(T) thin film, was developed, in which the crack length and crack closure were monitored by the compliance method utilizing a high–resolution laser displacement meter and data processing technique for noise elimination. By utilizing this system, we investigated the effects of grain size, specimen thickness, and force ratio on the fatigue crack propagation behavior of 5- and 10-μm-thick electrodeposited nanocrystalline nickel films, ultrafine-grained nickel films, a medium-size-grained nickel film, and a bulk nickel plate. Then, the effects of grain size, specimen thickness, and force ratio were examined and the role of crack

closure in these effects was examined. For a specimen with small width, it is impossible to obtained the threshold condition using the force shedding rate designated in ASTM E647-15 because of the conservativeness of this designation. To obtain the threshold values of specimens with small width, the validity of a high force shedding rate was confirmed using a bulk C(T) specimen. The results for thin films were compared with those reported by other groups to clarify the validity of the present system.

2. Materials and Experimental Procedure

2.1. Specimens

The shape and dimensions of the (a) C(T) and (b) SE(T) specimens are shown in Fig. 1, where the C(T) specimen was made of a commercially pure nickel plate with a thickness of 1.5 mm, named the MG plate, and the SE(T) specimen was made of either a medium-size-grained commercially pure nickel thin film, named the MG film or an electrodeposited nickel thin film, named nanocrystalline (NC) or ultrafine-grained (UFG). The initial notch with a length of 2.5 mm in the SE(T) specimen was formed using a utility knife, and the SE(T) specimen was glued to the grips of the test machine, where the distance between the edges of grips was set to 30.0 mm.

2.2. Materials

Nickel thin films were prepared by electrodeposition using sulphamate solution [25]. The composition of the solution in g/L was as follows: 250 $Ni(SO_3NH_2)_2$ (nickel sulphamate), 30 H_3BO_3 (boric acid), 10 $NiCl_2$ (nickel chloride), and 0.4 $CH_3(CH_2)_{10}CH_2OH$ (sodium lauryl sulphate). $C_3H_5NaO_3S$ (sodium allylsulfonate) at the amount of 0 or 0.8 g/L was added to the solution to control the microstructure of the electrodeposited thin films. A polished stainless-steel plate and a commercially pure nickel plate were employed as the substrate (cathode) and anode, respectively. The temperature of the hot-water circulation bath was maintained at 40°C. The pH of the solution was maintained at 4.0 by adding H_2NO_3S (sulphamate acid). The solution was stirred with a magnetic stirrer to prevent pit formation. The current density was maintained at 0.25 mA/mm^2 by supplying a constant current. The deposition times were 15 and 30 min to obtain the thicknesses of 5 and 10 μm, respectively.

After deposition, the thin films were removed from the substrate (cathode plate) and used in the fatigue crack propagation test as free-standing films. The inverse pole figure (IPF) maps obtained by electron backscatter diffraction (EBSD) analysis of the electrodeposited thin films with thicknesses of 5 and 10 μm, the MG thin film with a thickness of 10 μm, and the bulk MG plate with a thickness of 1.5 mm are shown in Figs. 2 and 3, where the film obtained by adding sodium allylsulfonate at the

amount of 0.8 g/L is named the NC thin film; the UFG thin film was fabricated without adding sodium allylsulfonate. As shown in Fig. 2, the grains in the NC thin film are randomly orientated in all directions. Grains on the substrate side of the UFG thin film are also randomly oriented, whereas those on the solution side have a texture with the (001) axis in the direction normal to the film surface. The microstructure of the solution-side surface of the 5-μm-thick film is similar to that of the midsection of the 10-μm-thick film. The orientation of grains in the bulk MG plate is also random.

The grain sizes on the solution side are 0.186 μm for the NC thin film, 0.789 μm for the UFG thin film, and 17.0 μm for the bulk MG plate [53]. In the UFG thin film, the grain size on the solution side is larger than that on the substrate side, whereas a similar structure to the solution side is dominant. Since the IPF maps of the MG thin film shown in Fig. 3 (a) indicate a poor quality owing to its high dislocation density, it is difficult to evaluate the grain size of the MG thin film. Since the number of grains contained in the same area in Figs. 3 (a) and (b) is almost the same, the average grain size of the MG thin plate must be almost the same as that in the MG plate (17.0 μm). On the other hand, grains in MG film are elongated along the rolling direction, which is perpendicular to the loading direction. The 0.2 % proof strength and tensile strength are 1065 MPa and 1690 MPa for the NC thin film and 469 MPa and 768 MPa for the UFG thin film, respectively [53].

To elucidate the effects of nanocrystallization and thickness on the fatigue crack propagation behavior, C(T) specimens made of commercially pure nickel with a width of 18 mm and a thickness of 1.5 mm were also prepared for comparison.

2.3. Fatigue test

The crack propagation tests were conducted under stress-intensity-factor-range (ΔK)-controlled conditions using a computer-controlled electrodynamic testing machine. The appearance of the fatigue test machine and the configuration of the system are shown in Figs. 4 and 5, respectively, where the loading capacities were 50 N for the SE(T) specimen, and 500 N for the C(T) specimen. The test system was set on an antivibration table in a sound-shielded room. The room temperature was controlled to 24±1 ºC. The accuracy and linearity of each load cell (Showa Measuring Instruments RCB-50N and RCB-500N) were better than ±1 % and 0.15 % of the rated output, respectively. The range and linearity of the laser displacement meter (KEYENCE LK-H025) were ±3 mm and 0.12 μm, respectively. Displacement between the specimen grips was measured using a caliper with the resolution of 0.01 mm. The resolution of the travelling microscope used for the optical measurement of crack length and initial notch length was 0.01 mm. The thickness of specimen was measured using a high-accuracy micrometer (Mitutoyo, Digimatic micrometer) with the resolution of 0.1 μm. Sinusoidal loading waves with force ratio R ranging from 0.1 to 0.7 at the frequencies (f) of 10 Hz for the SE(T) specimen and 60 Hz for the C(T) specimen were employed for cyclic loading.

The crack lengths were continuously monitored in terms of compliance between the applied force and the loading point displacement, *i.e.*, displacement between the grips, for the SE(T) specimen. For the C(T) specimen, the back-face strain was measured to determine the crack length by the compliance method. The crack closure behavior was also monitored by the compliance method for both specimens. The compliance $C = \mathrm{d}V/\mathrm{d}P$ (SE(T) specimen) or $\mathrm{d}\varepsilon_b/\mathrm{d}P$ (C(T) specimen) is defined as the inverse slope of the linear part of the relationship between the applied force P and the displacement between grip ends, V, or the back-face strain ε_b. V was measured using a high-resolution laser displacement meter, and ε_b was measured using a strain gage with a length of 2.0 mm glued to the back face of the specimen.

The stress intensity factor K and compliance C for the SE(T) specimen under pin loading, *i.e.*, without a remotely applied bending moment, can be found in handbooks [54, 55] and given in a simple form. Since pin loading is not possible for thin films, the specimen is usually glued to the grips of the test machine. In this case, rotation of the specimen at the grips is not allowed. Therefore, the specimen is subjected to not only the applied force, but also the bending moment from the grips. The stress intensity factor K and compliance C for the SE(T) specimen under fixed end displacement without rotation can be calculated as follows [56].

$$K = \frac{P\sqrt{\pi a}}{BW} F_{\mathrm{P}}(\xi)\left[1 - \frac{6}{W}\left(\frac{WI_{\mathrm{PM}}(\xi)}{L/W + 6I_{\mathrm{M}}(\xi)}\right)\frac{F_{\mathrm{M}}(\xi)}{F_{\mathrm{P}}(\xi)}\right] \tag{1}$$

$$C = \frac{V}{P} = \frac{1}{EB}\left[\frac{L}{W} + 2I_{\mathrm{P}}(\xi) - \frac{12I_{\mathrm{PM}}(\xi)^2}{\frac{L}{W} + 6I_{\mathrm{M}}(\xi)}\right] \tag{2}$$

Here, W is width, B thickness, a crack length, P applied force, V loading point displacement, L gauge length (distance between grips), E Young's modulus, $\xi = a/W$, and

$$\left.\begin{aligned} F_{\mathrm{P}}(\xi) &= \sqrt{\frac{2}{\pi\xi}\tan\left(\frac{\pi\xi}{2}\right)}\,\frac{0.752 + 2.02\xi + 0.37\left\{1 - \sin\left(\frac{\pi\xi}{2}\right)\right\}^3}{\cos\left(\frac{\pi\xi}{2}\right)} \\ F_{\mathrm{M}}(\xi) &= \sqrt{\frac{2}{\pi\xi}\tan\left(\frac{\pi\xi}{2}\right)}\,\frac{0.923 + 0.199\left\{1 - \sin\left(\frac{\pi\xi}{2}\right)\right\}^4}{\cos\left(\frac{\pi\xi}{2}\right)} \end{aligned}\right\} \tag{3}$$

$$\left.\begin{aligned} I_{\mathrm{P}}(\xi) &= \exp(8.68\xi - 3.896) \\ I_{\mathrm{M}}(\xi) &= \exp\left(6.570\xi - 3.846\right) \\ I_{\mathrm{PM}}(\xi) &= \exp\left(7.613\xi - 3.872\right) \end{aligned}\right\} \quad (0.25 \le \xi \le 0.75). \tag{4}$$

In most of previous works, the stress intensity factor K was analyzed by the finite-element

method (FEM) for a fixed L/W value.

The stress intensity factor K and the compliance $C = \varepsilon_b/P$ for the C(T) specimen were calculated using [54,55],

$$K = P / B\sqrt{W} \cdot F(\xi) \tag{5}$$

$$F(\xi) = \frac{(2+\xi)(0.886+4.64\xi-13.32\xi^2+14.72\xi^3-5.6\xi^4)}{\sqrt{(1-\xi)^3}} \tag{6}$$

$$a = \left(1.0386 - 2.7616C_n + 1.5008C_n^2\right)W, \tag{7}$$

where ε_b is the strain at 'Point A' in Fig. 1 (a), and

$$C_n = 1/\left(\sqrt{ECBW}+1\right). \tag{8}$$

For both specimens, Young's modulus was determined from the measured initial compliance and the initial crack length $a_{act,ini}$ which was measured by optical microscopy, to ensure that the calculated initial crack length $a_{cal,ini}$ agreed with $a_{act,ini}$. Since the crack length is not given as an explicit function of the compliance, it was calculated by the Newton–Raphson method using Eq. (2), where the derivative of Eq. (2) was calculated numerically. After the fatigue crack propagation test, the crack length calculated using Eqs. (2) and (7), a_{cal}, was modified by the following equation to ensure that the modified final crack length agreed with that measured by optical microscopy, $a_{act,fin}$.

$$a = \frac{a_{act,fin} - a_{act,ini}}{a_{cal,fin} - a_{cal,ini}}\left(a_{cal} - a_{cal,ini}\right) + a_{act,ini} \tag{9}$$

where $a_{cal,fin}$ is the calculated final crack length. Owing to the definition of E, $a_{cal,ini} = a_{act,ini}$.

Figure 6 shows the relationship between the compliance and crack length for the SE(T) specimen under the condition of fixed end displacement and for the C(T) specimen. The change in compliance with crack extension for the SE(T) specimen is much less than that for the C(T) specimen, indicating that a special technique is required for measuring the crack length and crack closure of the SE(T) specimen. The change in the compliance of the SE(T) specimen with the width of 10 mm upon a 50 μm extension of the crack was evaluated from Eq. (2), and the results are shown in Table 1. Since this extension occurs under a constant applied force range in a stepped force shedding test, the change in compliance means a change in the displacement range, indicating that less than 0.25 % accuracy is required to detect 50 μm extension of crack. Since the intensity of white noise can be eliminated by averaging, both force and displacement signals at the same phase were superimposed for more than 1000 successive cycles. The noise level can be reduced to less than $1/\sqrt{1000}$ times [57, 58]. After the averaging, both force and displacement signals were parabolically smoothed by simplified least-squares procedures proposed by Savitzky and Golay [57, 59]. This method involves fitting a second-order polynomial to sets of seven successive data points, where each signal had 287

data points in each cycle.

The fatigue crack propagation tests were conducted in ambient air with decreasing ΔK while keeping the force ratio R constant using a control computer that automatically reduced the force range immediately after the calculated crack extension Δa_{cal} at each applied force step exceeded 50 μm for the SE(T) specimen, where R is the ratio of the minimum applied force to the maximum applied force during one fatigue loading cycle. The force shedding rate k defined by the following equation was determined to be -0.30 mm^{-1} for the SE(T) specimen; this leads to the force reduction rate at each crack extension Δa_{cal} of 50 μm being 1.5 %.

$$k = \left(\frac{1}{\Delta K}\right) \cdot \left(\frac{d\Delta K}{da}\right) \tag{10}$$

For the C(T) specimen, Δa_{cal} was either 25 or 50 μm, and k was -0.08, -0.4, or -0.8.

The force shedding procedure is illustrated in Fig. 7, and was conducted using the calculated crack length. Force shedding was performed the first time when the calculated crack extension exceeded the predetermined value, Δa_0, or the elapsed time Δt exceeded 10 h. Because there are small differences between the actual crack length and the calculated crack length and between Δa_{cal} and Δa_0, force shedding was not strictly conducted at the predetermined value of k in Eq. (10). However, as will be described later, k did not affect the da/dN–ΔK relationship for $-0.08 \geq k \geq -0.8$.

In the analysis of the da/dN–ΔK relationship, the average crack length was employed where the modified crack length was averaged over each Δa_0 interval. da/dN was calculated by the incremental polynomial method. This method involves fitting a second-order polynomial to sets of five successive data points. The crack propagation rate da/dN was obtained from the derivative of the above polynomial, as recommended in ASTM E647-15.

In the fatigue crack propagation test, the modified crack length at the threshold was equal to the final crack length measured by optical microscopy; then, the threshold stress intensity factor range was always evaluated using the optically measured crack length and measured applied force.

3. Experimental Results

3.1. Crack length and closure measurement of SE(T) specimen

Figure 8 shows examples of the force–displacement curves obtained by the force shedding fatigue crack propagation test of the SE(T) specimen under the loading frequency of 10 Hz. These curves were obtained by averaging over 1000 cycles to eliminate electrical noise. Every curve shows strange behavior around the mean force position, where the speed of specimen movement was the highest under sinusoidal loading. To confirm that this strange behavior is due to the high-speed movement of the specimen, the effect of loading frequency was examined, and we found by

comparing Figs. 8 and 9 that the strange behavior attenuated with decreasing loading frequencies. Neither mechanical loosening nor wrinkling of the film could be responsible for the strange behavior because it occurs at a different force level and depends on the loading frequency. One possible cause of this strange behavior is the fluttering of the film at the crack mouth owing to the movement of the film in air; this may generate aerodynamic force such as a Karman vortex.

There is a slight difference in the slopes of the P–V relationship between the regions higher and lower than the strange behavior. This difference is attributed to a change in rigidity caused by factors other than crack propagation and/or crack closure. However, the change in rigidity can be made negligible by correcting Young's modulus so as to match the initial calculated crack length with the actual initial crack length. Then, the compliance C is evaluated in a region higher than the strange region to calculate crack lengths using Eqs. (2), (3), and (4). These are indicated by circles in Fig. 10, and diamonds indicate the modified crack length obtained using Eq. (9), where the actual crack length was measured by optical microscopy during the fatigue crack propagation test. The difference between the actual and calculated crack lengths was found to be less than 0.46 mm, and the average difference was 0.26 mm with the standard deviation of 0.15 mm. This result was obtained by interrupting the fatigue tests for the optical measurement of crack length, which induced additional error. In continuous monitoring, the scatter of data may be smaller than that indicated in Fig.10, but systematic error may still exist.

The accuracy of the present method must be independent of specimen thickness because the displacements are identical for two specimens of different thicknesses subjected to the same stress intensity factor (under small scale yielding) with a similar two-dimensional shape including crack length. Consequently, an appropriate load cell should be employed because the applied force for the same stress intensity factor is proportional to the specimen thickness; however, the condition given by Eq. (10) restricts the limitation of specimen width, *i.e.*, for specimens with small width, crack length reaches the specimen width before reaching the threshold condition.

Figure 11 shows an example of a crack propagation curve where the modified crack length was averaged over each Δa_0 interval. Although the standard deviation from the seventh-order polynomial regression curve is 25 μm, further systematic deviation from the actual crack length may exist. However, no serious error is observed in the measurement of the threshold stress intensity factor range because the modified final crack length calculated using Eq. (9) is exactly the same as the crack length measured by optical microscopy.

The crack closure behavior was evaluated after the fatigue crack propagation test. An example of the measured crack opening force used to determine the effective stress intensity factor range ΔK_{eff} is shown in Fig. 12. ΔK_{eff} was obtained under the threshold condition of the MG thin film at the force ratio R of 0.1. Figure 12 (a) is the force–displacement curve and Fig. 12 (b) shows the deviation of

displacement from the linear part of (a) indicated by the dashed line [60]. Here, linear approximation was performed above the applied force at which the crack is considered to be opened, and included the strange part to evaluate the crack opening force because the change in compliance due to crack opening was much larger than that due to crack closure.

Figure 12 (b) shows that the crack opening force, and hence the effective stress intensity factor range ΔK_{eff} of the SE(T) specimen, can be successfully evaluated by the compliance method.

3.2. Fatigue crack propagation behavior of bulk MG plate

The fatigue crack propagation behavior of the C(T) specimen is shown in Fig. 13, where (a) shows the relationship between the crack propagation rate da/dN and the stress intensity factor range ΔK and (b) shows the relationship between da/dN and ΔK_{eff}. ΔK and ΔK_{eff} were calculated by substituting ΔP and ΔP_{eff} for K in Eq. (5), where ΔP and ΔP_{eff} are defined in Fig. 12 (b).

ASTM Standard E647-15 designates that k defined by Eq. (10) should be larger than -0.08. However, it is difficult to reach the threshold condition for a small specimen when employing $k \geq$ -0.08. The physical meaning of $k \geq$ -0.08 is that the force shedding rate

$$\frac{P_{\max 1} - P_{\max 2}}{P_{\max 1}} \approx -k\Delta a_0 \leq 0.02 \qquad (11)$$

should be satisfied when each crack extension Δa_0 is 250 μm, where P_{1max} and P_{max2} are the applied forces before and after force shedding, respectively. ASTM E647-15 designates that a rate lower than 0.02 given by Eq. (11) corresponds to continuous force shedding.

To ensure a valid da/dN–ΔK relationship with more rapid ΔK shedding, the condition given by Eq. (11) was maintained whereas the effects of k and the shedding interval Δa_0 were examined for more rapid ΔK shedding. The results for R = 0.1 shown in Fig. 13 prove that an almost unique da/dN–ΔK relationship can be obtained as long as the condition given by Eq. (11) is satisfied and $k <$ -0.08. Then, k = -0.4 and Δa_0 = 50 μm were employed in experiments at other force ratio R values for the C(T) specimen, and k = -0.3 and Δa_0 = 50 μm for the SE(T) specimen.

Figure 13 (a) shows that the crack propagation rate da/dN at the same ΔK is higher and the threshold stress intensity factor range ΔK_{th} is lower at higher force ratios, although no effect of the force ratio is observed in the da/dN–ΔK_{eff} relationship, as shown in Fig. 13 (b), indicating that the effect of the force ratio can be attributed to crack closure [10, 61]. Figure 14 shows the stress intensity factors under the threshold conditions, $K_{max,th}$, $K_{min,th}$, and $K_{op,th}$ as a function of R, where the subscripts mean the values at the maximum force, minimum force, and crack opening force in each loading cycle, respectively. Since $K_{max,th}$ and $K_{op,th}$ are constant independent of R for $K_{min,th} \leq K_{op,th}$, $\Delta K_{eff,th} = K_{max,th} - K_{op,th}$ is also independent of R, although ΔK_{th} depends on R. The invariance of $K_{op,th}$ strongly supports the roughness-induced crack closure mechanism [62].

3.3. Fatigue crack propagation behavior of thin film

Figure 15 shows the da/dN–ΔK relationships of the electrodeposited thin films with a thickness of 10 μm, where (a) and (b) show the relationships for the UFG and NC thin films, respectively. For both materials, the force ratio R showed no effect because the crack did not close, as shown in Fig. 16; then, $\Delta K = \Delta K_{\mathrm{eff}}$.

The da/dN–ΔK relationships were examined for the films with thicknesses of 5 and 10 μm under the force ratio R of 0.1, as shown in Fig. 17. There is no effect of the specimen thickness. Since no crack closure was observed in films of either thickness, ΔK_{eff} was equal to ΔK.

Figures 18 (a) and (b) show the effects of force ratio on da/dN–ΔK and da/dN–ΔK_{eff} relationships for the MG thin film with a thickness of 10 μm. The da/dN–ΔK relationship depends on the force ratio R, whereas the effect of R on the da/dN–ΔK_{eff} relationship is negligible under the threshold condition. As shown in Fig. 12, the crack closure behavior was observed at R=0.1, showing that crack closure occurred in the thin film with the medium grain size (MG).

4. Discussion

The da/dN–ΔK and da/dN–ΔK_{eff} relationships obtained in the present study are shown in Fig. 19, for (a) R = 0.1 and (b) R = 0.5. The relationships for the thin films are much different from those for the bulk MG plate, *i.e.*, the crack propagation rate of the thin films is almost tenfold that of the bulk MG plate at comparable ΔK or ΔK_{eff}. Note that the da/dN–ΔK relationship for the NC and UFG thin films does not depend on the force ratio R, as shown in Fig. 15. The crack propagation behavior of the MG thin film is similar to those of the NC and UFG thin films in the Paris law region; however, the da/dN–ΔK_{eff} relationship of the MG thin film approaches that of the bulk MG plate in the region near threshold, although there is a significant difference in the da/dN–ΔK relationship. This indicates that crack closure is responsible for the effect of thickness under the threshold condition.

The threshold stress intensity factor range ΔK_{th} of the nanocrystalline thin film depends on microstructural characteristics such as grain size, whereas $\Delta K_{\mathrm{eff,th}}$ of the MG thin film seems to be comparable to that of the bulk MG plate. Since ΔK_{th} of the MG thin film is lower than that of the bulk MG plate, the crack closure behavior depends on the specimen thickness.

The da/dN–ΔK relationships under R=0.1 for various pure nickel [22–25] and Ni–1 % Co [26] thin films and the bulk nickel plate are shown in Fig. 20. In the present study and Tanaka et al.'s study, thin films with a thickness of 10 μm were employed, whereas thicknesses of other films were in the range from 100 to 180 μm. In all regions, the crack propagation rate is always higher for thin films than for the bulk plate in the same stress intensity factor range, and the threshold stress intensity factor range for thin films is lower than that of the bulk plate. In the Paris law region where

441 da/dN>1.0×10^{-8} (m/cycle) (Region B), the effect of grain size on the da/dN–ΔK relationships is
442 minimal for the results obtained from the 10-μm-thick film; however, the crack propagation rate is
443 higher for films with smaller grain size and thicknesses from 100 to 180 μm. A comparison of the
444 results for NC films shows the crack propagation rate of the 100-μm-thick film (Harlon et al. [23]
445 and Xie et al. [24]) to be higher than that of the 10-μm-thick film (present study and Tanaka et al.
446 [25]). Results for UFG films show a similar tendency. For MG films, the crack propagation rate is
447 almost the same for the 10-μm-thick film (present study) and the 180-μm-thick film (Xie et al. [24])
448 at da/dN > 10^{-7} m/cycle; however, da/dN for the bulk plate (present study) is considered to be lower
449 than that for thin films.
450 Results shown in Fig. 20 indicate that the cack propagation rate in thin films is higher than that
451 in the bulk plate, but between thin films, the rate is lower for the thinner film. The effect of specimen
452 thickness has been discussed in terms of plane-stress and plane-strain conditions, and the crack
453 propagation in thin films and the bulk plate is also considered under plane-stress and plane-strain
454 conditions, respectively. The front of fatigue cracks is usually curved as a result of the retardation of
455 crack propagation at the surface. This indicates that the crack propagation resistance under the plane-
456 stress condition is higher than that under the plane-strain condition, contrary to the present results.
457 This phenomenon seems to be similar to the 'breakdown' of the similitude concept in short cracks
458 because reductions of both the crack length and specimen thickness bring about a decrease in crack
459 area.
460 The exponent in the Paris law for a pure nickel thin film is four, whereas it is typically between
461 two and four for conventional ductile alloys [63]. Even in the Paris law region, the fatigue crack
462 propagation rate of Ni–1 %Co is much lower than that of pure nickel and the exponent is 1.6, showing
463 that alloying contributes to the enhancement of the fatigue crack propagation resistance.
464 In the region near the threshold (Region A), da/dN is higher and ΔK_{th} is lower for films with
465 smaller grain size; however, ΔK_{th} for the UFG film in the present study is almost identical to that for
466 the NC film used by Tanaka et al. [25], and ΔK_{th} for the MG film in the present study is almost
467 identical to that for the UFG film used by Tanaka et al. [25] indicating that ΔK_{th} is not solely
468 dependent on grain size. Other factors, such as grain boundary stability [53, 64], also affect ΔK_{th}.
469 The effect of the thickness of the thin film could not be clarified because data were obtained
470 only for specimens with a thickness of 10 μm; however, we found that da/dN is higher and ΔK_{th} is
471 lower for the MG thin film than those for the MG bulk plate. As shown in Fig. 19 (b), this difference
472 can be explained by crack closure.
473 It is well known that for conventional materials, ΔK_{th} and Δ$K_{eff,th}$ increase linearly with the
474 square root of grain size, $d^{1/2}$, as reported by Nakai et al. [10]. Taira et al. [65] analyzed the effect of
475 grain size on the threshold condition using the blocked slip band model, in which the threshold

condition is determined whether or not the slip band emanating from the crack tip can penetrate the grain boundary ahead of the crack tip. They found this condition to be controlled by the microscopic stress intensity factor at the tip of the slip band emanating from the crack tip and predicted that $\Delta K_{eff,th}$ increases linearly with the square root of grain size, $d^{1/2}$. ΔK_{th} and $\Delta K_{eff,th}$ of the present materials are plotted as a function of $d^{1/2}$ in Fig. 21. $\Delta K_{eff,th}$ is independent of specimen thickness for MG, and linearly increases with the square root of the grain size. However, ΔK_{th} of MG depends on the specimen thickness, indicating that the thickness effect on ΔK_{th} of MG can be attributed to the difference in crack closure, *i.e.*, the crack opening stress intensity factor K_{op} decreases with decreasing specimen thickness in the case of a long crack, similarly to the physically/mechanically short crack, in which K_{op} decreases with decreasing crack length.

Minakawa et al. [66] found that K_{op} is related to the roughness of the fracture surface, and Sadananda et al. [67] reported that coarse microstructures are related to crack paths, which in turn promote resistance to the propagation of fatigue cracks via crack closure due to roughness. To examine the effect of the roughness of the fracture surface, the side surface of the specimen was observed. Figures 22 and 23 indicate that the tortuosity of the crack path in the NC thin film is lower than that in a film with larger grain size (UFG) regardless of the crack propagation rate and stress ratio. However, the differences between the UFG and MG thin films are not clear.

The fractographies of the thin films are shown in Figs. 24 and 25. The fracture surface of the NC thin film is very flat compared with that of the UFG thin film regardless of crack propagation rate and force ratio. No significant difference in the appearance of the fracture surface between the solution and substrate sides is recognized in the NC thin films, whereas the roughness is greater on the solution side than on the substrate side, which is consistent with the microstructural observation shown in Fig. 2, indicating that the grain size on the solution side is larger than that on the substrate side. Note that the roughness in the crack propagation direction is greater for the electrodeposited thin film and the roughness in the thickness direction is greater for the MG thin film, *i.e.*, perpendicular to the electrodeposited direction and perpendicular to the rolling direction, respectively.

5. Conclusions

We developed experimental techniques for measuring the crack length and crack closure behavior of a SE(T) specimen with fixed ends by compliance method, employing a high-resolution laser displacement meter and a data processing technique for noise elimination. By utilizing this system, we developed an automatic force-shedding fatigue crack propagation test system to examine the fatigue crack propagation behavior of the SE(T) thin film specimens with thicknesses of 5 and 10 μm and a width of 10 mm, and a bulk C(T) specimen. The results were compared with previous results obtained from films with thicknesses from 100 to 180 μm. The effects of grain size, specimen

thickness, and force ratio on fatigue crack propagation behavior were examined for electrodeposited nanocrystalline and UFG nickel thin film, medium-size-grained rolled thin film, and a bulk plate with a thickness of 1.5 mm. The following results were obtained.

1. The crack length can be measured by the compliance method, and the crack closure behavior of the SE(T) thin films with thicknesses of 5 and 10 μm could be measured by the compliance method using a high-resolution laser displacement meter together with averaging over more than 1000 cycles and smoothing of both the displacement and applied force signals. The difference in crack length between the compliance and visual methods was 0.46 mm at maximum and 0.26 mm on average with the standard deviation of 0.15 mm.
2. The da/dN–ΔK relationship for the bulk C(T) specimen obtained by the force-shedding test was not affected by the shedding rate from -0.8 to -0.08, where the force shedding rate at each step was kept at less than 2 %.
3. The relationship between the crack propagation rate da/dN and the stress intensity factor range ΔK for the NC and UFG thin films with thickness of 5 and 10 μm was independent of the force ratio.
4. In the Paris law region, no effect of grain size on the da/dN–ΔK relationship was observed for the 10-μm-thick film; however, da/dN of the NC film was higher than that of the UFG film at comparable ΔK for films with thicknesses from 100 to 180 μm. The threshold stress intensity factor range ΔK_{th} of 10-μm-thick films with smaller grain size was lower.
5. The da/dN–ΔK relationship for the 10-μm-thick film was always identical to that for the 5-μm-thick film; however, da/dN of the 100μm-thick-film was higher than that of the 10-μm-thick film for both NC and UFG films. On the other hand, the rate of the MG thin film was higher, and ΔK_{th} of the 10-μm-thick film was lower than that of the bulk plate.
6. No crack closure was observed in the UFG or NC thin films, whereas it occurred in the MG thin film with a thickness of 10 μm and in the bulk MG plate. The da/dN–ΔK_{eff} relationships for thin films were independent of the force ratio and film thickness. In the Paris law region, da/dN for the MG film was higher than that for the MG plate at comparable ΔK_{eff}, indicating that crack closure could not account for the thickness effect. However, $\Delta K_{eff,th}$ of the MG film was almost identical to that of the MG plate.
7. The acceleration of crack propagation in thin films in the Paris law region shows the breakdown of the similitude concept, as similarly observed for the microstructurally short crack combined with the crack closure issue similar to that of the physically/mechanically short crack.

Acknowledgement

Supports of this work through by Grant-in-Aid for Challenging Exploratory Research (JSPS KAKENHI Grant Number 25630014) and Grant-in-Aid for Scientific Research (C) (JSPS KAKENHI

Grant Number 18K03837) are gratefully acknowledged. The authors would like to thank Mr. R. Takeshige (Graduate School, Kobe University) and K. Fujita (Graduate School, Shizuoka University) for their technical support.

References

[1] Gleiter H. Nanostructured materials: basic concepts and microstructure, Acta Mater 2000;48: 1-29.

[2] Meyers MA, Mishra A, Benson DJ. Mechanical properties of nanocrystalline materials. Progress in materials science, 2006:427-556

[3] Dao M, Lu L, Asaro RJ, Hosson JTMD, Ma E. Toward a quantitative understanding of mechanical behavior of nanocrystalline metals. Acta Mater 2007;55:4041-4065.

[4] Padilla HA, Boyce BL. A review of fatigue behavior in nanocrystalline metals. Exp Mech 2010;2010;50 : 5–23.

[5] Kumar KS, Swygenhoven HV, Suresh S. Mechanical behavior of nanocrystalline metals and alloys. Acta Mater 2003;51: 5743-5774.

[6] Thompson AW. Effect of grain size on work hardening in nickel. Acta Metallur 1977;25:83-86.

[7] Taira S, Tanaka K, Hoshina M. Grain size effect on crack nucleation and growth in long-life fatigue of low-carbon stee. ASTM STP 675 1979;135-173.

[8] El-Sherik AM, Erb U. Synthesis of bulk nanocrystalline nickel by pulsed electrodeposition. J Mater Sci 1995;30:5743-5749.

[9] Ebrahimi F, Bourne GR, Kelly MS, Matthewa TE. Mechanical properties of nanocrystalline nickel produced by electrodeposition. Nanostruct Mat 1999;11:343-350.

[10] Nakai Y, Tanaka K, Nakanishi T. The Effects of Stress Ratio and Grain Size on Near-threshold Fatigue Crack Propagation in Low-carbon Steel, Eng Fract Mech 1981;15: 291-302.

[11] Donald JK. Fatigue crack propagation and the role of automated testing. ASTM Standardization News 1985; 50-53.

[12] Beevers, C.J. The Measurement of crack length and shape during fracture and fatigue. Engineering Materials, Advisory Service, West Midlands, U.K. (1980).

[13] Wei RP, Brazill RL. An assessment of A-C and D-C potential system for monitoring fatigue crack growth. ASTM STP 738, 103-119 (1981).

[14] Tanaka K, Wei RP. Short fatigue crack growth of HYI30 steel in 3.5% NaCl solution. Eng Fracture Mech 1985;21: 295-305.

[15] Nakai Y, Tanaka K, Wei RP, Short-crack growth in corrosion fatigue for a high strength steel. Eng Frac Mech 1986; 24: 433-444.

[16] Nakai Y, Akagi H, Kitamura Y, Ohji K, Measurement of surface crack lengths by an AC

potential method. Trans Jpn Soc Mech Eng 1989; 55: 543-549.
[17] Nakabo S, Ueno A, Maeda Y, Fukuchi S, Ogami J. Proposal to evaluate fatigue crack propagation tests with piston displacement aided compliance technique and evaluation of fatigue crack propagation properties of SCM435 in ultra high-pressure H_2 gas. J Soc Mat Sci Jpn 2020; 69: 889-894.
[18] Sharpe WN. Su X. Closure measurements of naturally initiating small cracks, Eng Frac Mech 1988; 30: 275-294.
[19] Nakai Y and Ohji K. Predictions of growth rate and closure of short fatigue cracks. Short Fatigue Cracks (ESIS 13), K.J.Miller and E.D. Los Rios, eds., Mechanical Engineering Publications, London, 169-189 (1992).
[20] Ohji K, Kubo S, Nakai Y, Tamura E, Shiotani S, Kacou TA. Near-threshold fatigue crack growth behavior of SUS304 steel at high temperatures using interferometric strain/displacement gage (1st report, crack closure behavior). JSME Int J (A) 1999; 42:90-96.
[21] Grünewald P, Rauber J, Marx M, Motz C, Schaefer F. Fatigue crack growth in micro specimens as a tool to measure crack–microstructure interactions, Fatigue Fract Eng Mater Struct 2020; 43: 3037-3049.
[22] Hanlon T, Kwon YN, Suresh S. Grain size effects on the fatigue response of nanocrystalline metals, Scripta Mater 2003;49: 675-680.
[23] Hanlon T, Tabachnikova ED. Suresh S. Fatigue behavior of nanocrystalline metals and alloys, Int J Fatigue 2005;27: 1147-1158.
[24] Xie J, Wu X, Hong Y. Shear bands at the fatigue crack tip of nanocrystalline nickel, Scripta Mater 2007;57: 5-8.
[25] Tanaka K, Sakakibara M, Kimachi H. Grain size effect on fatigue properties of nanocrystalline nickel thin films made by electrodeposition, Procedia Engineering 2011;10:542-547.
[26] Cavaliere P. Fatigue properties and crack behavior of ultra-fine and nanocrystalline pure metals. Int J Fatigue 2009; 31:1476-1489.
[27] Sangid MD, Pataky GJ, Sehitoglu H, Rateick RG. Superior fatigue crack growth resistance, irreversibility, and fatigue crack growth–microstructure relationship of nanocrystalline alloys, Acta Mater 2011;59: 7340-7355.
[28] Tong J, Alshammrei S, Lin B, Wigger T, Marrow T. Fatigue crack closure: A myth or a misconception?. Fatigue Fract Eng Mater Struct 2020; 42: 2747-2763.
[29] Suresh S, Ritchie RO, Propagation of short fatigue cracks, Int Met Rev 1984;29: 445-475.
[30] Tanaka K, Nakai Y, Maekawa M. Microscopic study of fatigue crack initiation and early propagation in smooth specimen of low carbon steel. J Soc Mat Sci Jpn 1982;
[31] Tanaka K, Hojo M, Nakai Y. Fatigue crack initiation and early propagation in 3% silicon iron.

Fatigue Mechanisms: Advances in Quantitative Measurement of Physical Damage, J. Lankford, D. L. Davidson, W. L. Morris, and R. P. Wei, eds., ASTM STP 811, 207-232 (1983).

[32] Hojo M, Tanaka K, Nakai Y. Etch-pit study of early fatigue crack propagation in 3% silicon iron. J Soc Mat Sci Jpn 1983; 32: 769-775.

[33] Tanaka K, Akiniwa Y, Nakai Y, Wei RP. Modelling of small fatigue crack growth interacting with grain boundary. Eng Frac Mech 1986; 24: 803-819.

[34] Nakai Y, Tanaka K. Grain size effect on growth threshold for small surface-cracks and long through-cracks under cyclic loading. Proceedings of the 23rd Japan Congress on Materials Research 1980; 106-112.

[35] Tanaka K, Nakai Y, and M. Yamashita. Fatigue growth threshold of small cracks. International Journal of Fracture 1981; 17: 519-533.

[36] Nakai Y, Tanaka K, Yamashita M. Analysis of closure behavior of small fatigue cracks. J Soc Mat Sci Jpn 1983; 32: 19-25.

[37] Nakai Y, Tanaka K, Kawashima R. Propagation and non-propagation of fatigue cracks in notched plates in low-carbon steel. J Soc Mat Sci Jpn 1983; 32: 535-541.

[38] Tanaka K, Nakai Y. Propagation and Non-propagation of short fatigue cracks at a sharp notch. Fatigue of Engineering Materials and Structures 1983; 6: 4, 315-327.

[39] Tanaka K, Nakai Y. Prediction of Fatigue Threshold of Notched Components. J Eng Mater Tech, Trans ASME 1984; 106: 192-199.

[40] Tanaka K, Nakai Y. Mechanics of growth threshold of small fatigue cracks. Fatigue Crack Growth Threshold Concepts, D. L. Davidson and S. Suresh, eds., The Metallurgical Society of AIME, Philadelphia, 497-516 (1984).

[41] Nakai Y and Ohji K. Prediction of growth rate of short fatigue cracks. Trans Jpn Soc Mech Eng A 1987; 53: 387-392.

[42] Maierhofer J, Kolitsch S, Pippan R, Gänser HP, Madia M, Zerbst U. The cyclic R-curve – Determination, problems, limitations, and application. Eng Frac Mech 2018; 198: 45-64.

[43] Gangloff RP. The criticality of crack size in aqueous corrosion fatigue. Res Mech Left 1981; 1; 299-306.

[44] Gangloff RP, Crack-size effects on the driving force for aqueous corrosion fatigue. Metal Trans (A) 1985; 16; 953-969.

[45] Gangloff RP, Oxygen inhibition model of the chemical crack size effect in corrosion fatigue. In Embrittlement by the localized crack environment (Edited by R. P. Gangloff), TMS-AIME, 265-290 (1984).

[46] Tanaka K, Wei RP, Growth of short fatigue cracks in HY130 steel in 3.5% NaCl solution, Eng Fract Mech 1985; 21: 293-305.

[47] Nakai Y, Tanaka K, Wei RP. Short-crack growth in corrosion fatigue for a high strength steel. Eng. Frac. Mech. 1986; 24; 433-444.
[48] Nakai Y, Alavi A, Wei RP. Effects of frequency and temperature on short fatigue crack growth in aqueous environments. Metallur Trans A 1988; 19A; 543-548.
[49] Shim G, Nakai Y, Wei RP. Corrosion fatigue and electrochemical reactions in steels. Basic Questions in Fatigue: Volume II, R.P. Wei and R.P. Gangloff, eds., American Society for Testing and Materials, Philadelphia, ASTM STP 924, 211-229 (1988).
[50] Nakai Y, Akagi H, Kitamura Y, Ohji K. Short surface crack growth of a high-strength low-alloy steel under cyclic loading in 3.5% NaCl solution. Trans Jpn Soc Mech Eng A 1989; 55: 1724-1732.
[51] Nakai Y, Ohji K. Short surface crack growth in corrosion fatigue. Fatigue 90, H. Kitagawa and T. Tanaka, eds., Materials and Component Engineering Publications Ltd., Birmingham, U.K., Vol. III, 1605-1610 (1990).
[52] Kondo T, Bi XC, Hirakata H, Minoshima K. Mechanics of fatigue crack initiation in submicron-thick freestanding copper films. Int J Fatigue 2016;82: 12-28.
[53] Nakai Y, Takeshige R, Hirai T, Kikuchi S. Effects of grain size and grain boundary stability on mechanical and fatigue properties of nanocrystalline nickel thin films. Mater Trans 2021.
[54] Tada H, Paris P, Irwin G. The analysis of cracks handbook. 3rd ed. New York: ASME; 2000.
[55] Murakami Y. ed. Stress intensity factor handbook. Kyoto: Committee on Fracture Mechanics, The Society of Materials Science, Japan; 1987.
[56] Nakai Y, Kubo S. Fracture Mechanics. Tokyo: Asakura Publishing; 2014:177-180.
[57] Nakai Y, Kubo S. Fracture Mechanics. Tokyo: Asakura Publishing; 2014:164-176.
[58] Skorupa M, Beretta S, Carboni M, Machniewicz T. An algorithm for evaluating crack closure from local compliance measurements. Fatigue Fract Eng Mater 2002;25:261-273.
[59] Savitzky A, Golay M. Smoothing and differentiation of data by simplified least squares procedures. Analytical Chemistry 1964;36:1627-1639.
[60] Kikukawa M, Jono M, Hora H. Fatigue crack propagation and closure behavior under plane strain condition. Int J Fract 1977;13:699-701.
[61] Nakai Y, Tanaka K, Kawashima R. Stress-ratio effect on fatigue crack growth threshold in steels. J Mat Sci Jpn 1984;33 (371):1045-1051.
[62] Nakai Y, Kikuchi S, Osaki K, Kawabata MO, Ameyama K. Effects of rolling reduction and direction on fatigue crack propagation in commercially pure titanium with harmonic structure. Int J Fatigue 2021;143:106018.
[63] Suresh. Fatifue of materials: Cambridge University Press; New York: 1991: 193.
[64] Hu J, Shi YN, Sauvage X, Sha G, Lu K. Grain boundary stability governs hardening and

softening in extremely fine nanograined metals. Science 2017;355: 1292-1296.
[65] Taira S, Tanaka K, Nakai Y. A model of crack-tip slip band blocked by grain boundary. Mech Res Comm 1978;5:375-381.
[66] Minakawa K, McEvilly AJ. On crack closure in the near-threshold region. Scripta Metallur 1981;15:633-636.
[67] Sadananda K, Vasudevan AK. Fatigue crack growth behavior of titanium alloys. Int J Fatigue, 2005;271255-1266.

690 **List of Figures**

691

MG plate for the present study.

Figure 21. Effect of grain size on fatigue crack propagation threshold.

Figure 22. Crack path in Region B (da/dN=1.0×10^{-8} m/cycle) of thin films.

Figure 23. Crack path in Region A (da/dN =1.0×10^{-10} m/cycle) of thin films.

Figure 24. Fracture surface in Region B (da/dN =1.0×10^{-8} m/cycle) of thin films.

Figure 25. Fracture surface in Region A (da/dN =1.0×10^{-10} m/cycle) of thin films.

Table 1. Change of compliance with Δa = 50 µm for W = 10 mm (SE(T)).

a (mm)	3.0	4.0	5.0	6.0	7.0
$\Delta C/C$ (%)	0.25	0.65	0.91	1.05	1.08

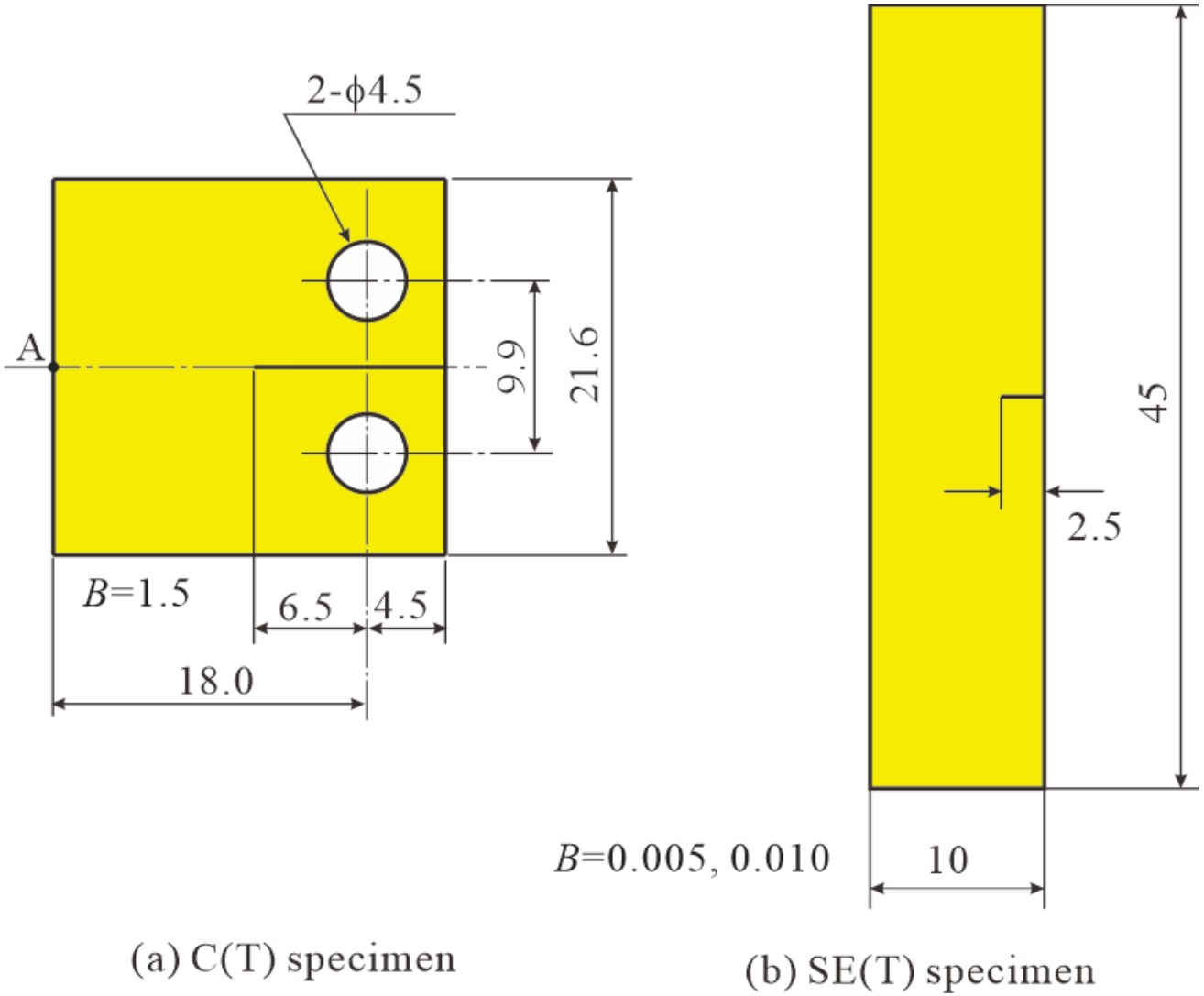

Figure 1. Shape and dimensions of specimens (in mm).

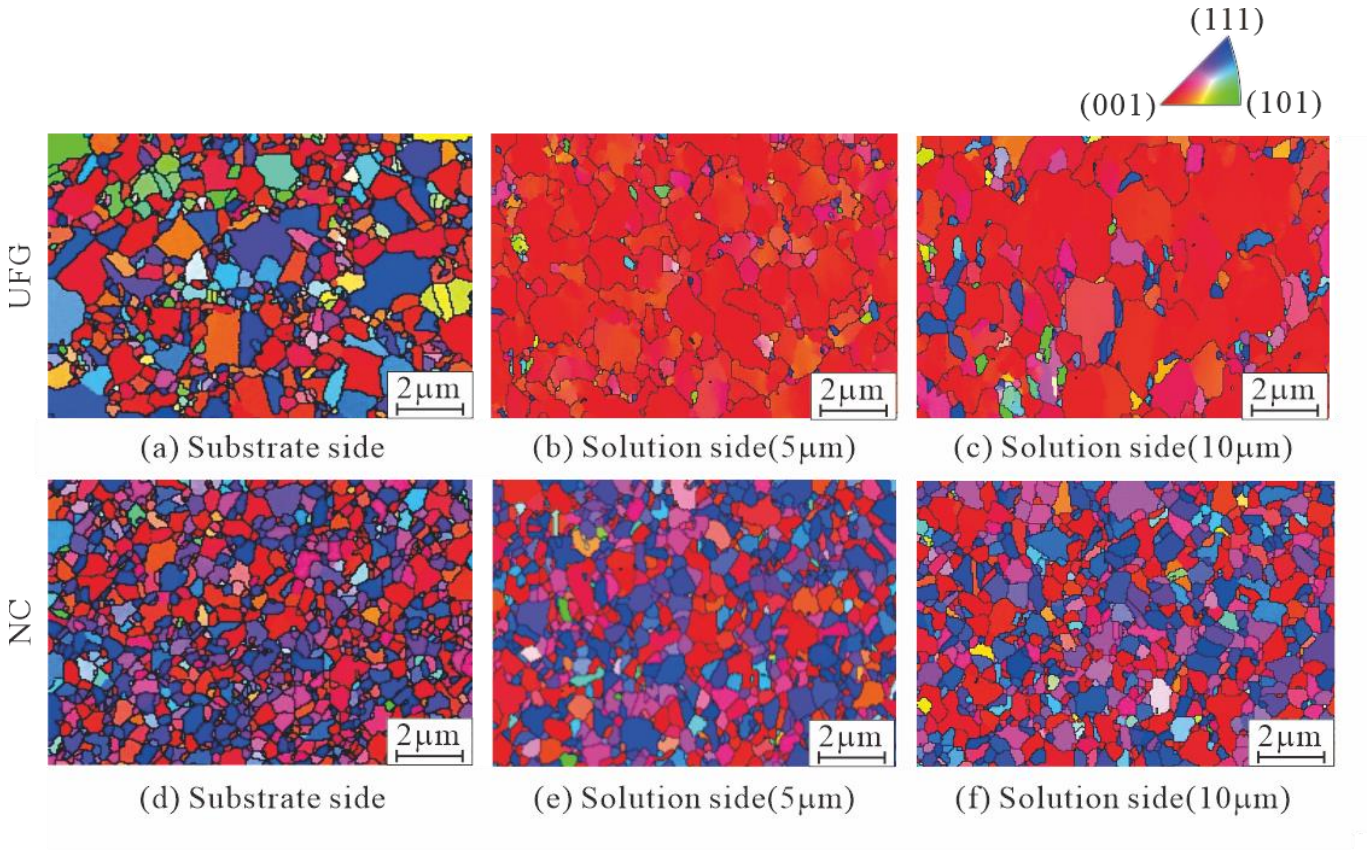

Figure 2. Inverse pole figure (IPF) maps of ultra-fine grained (UFG) and nanocrystalline (NC) electrodeposited films.

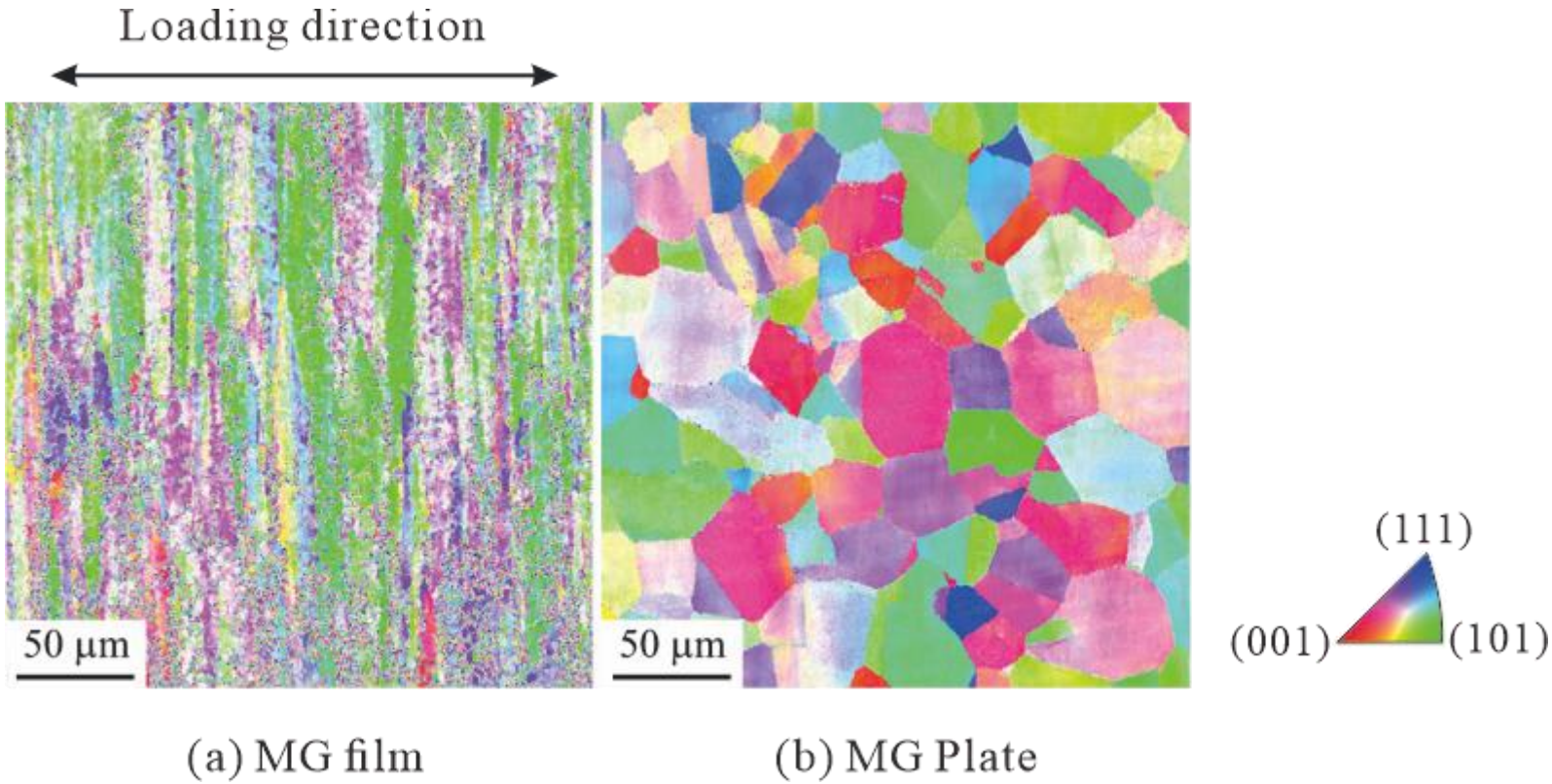

Figure 3. Inverse pole figure (IPF) maps of medium grain size (MG) material.

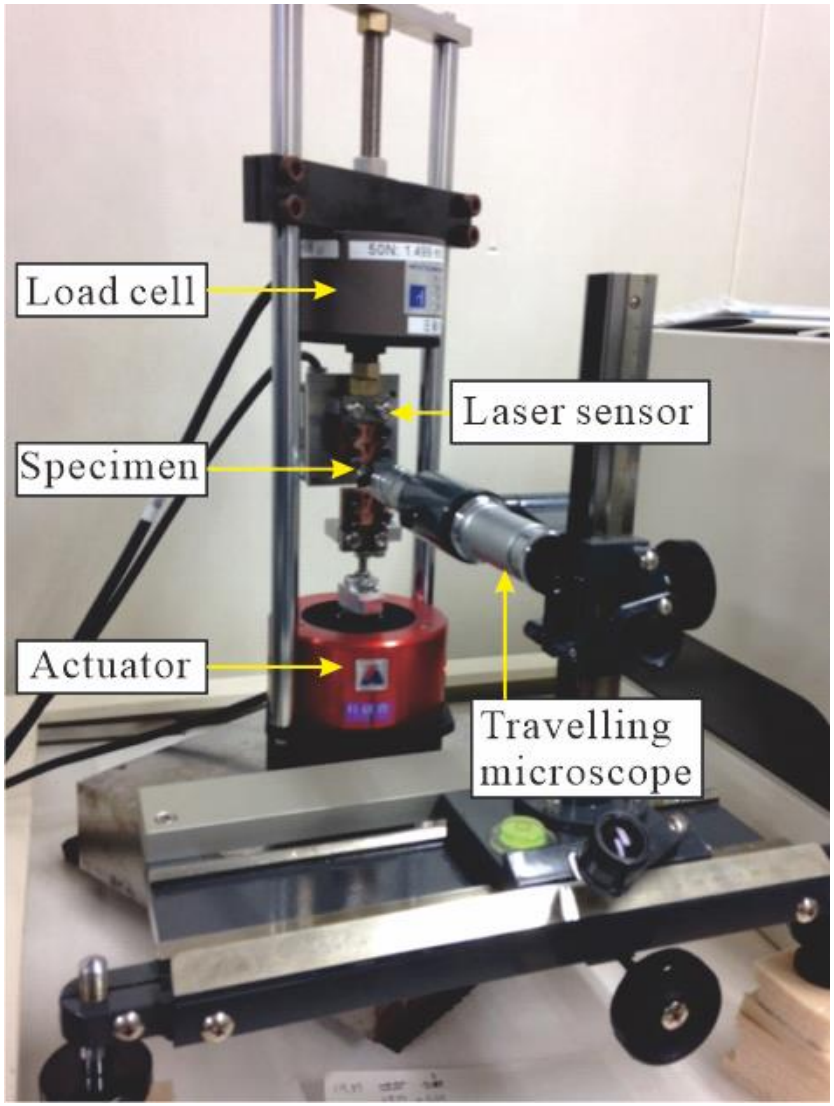

Figure 4. Appearance of fatigue test machine for thin film.

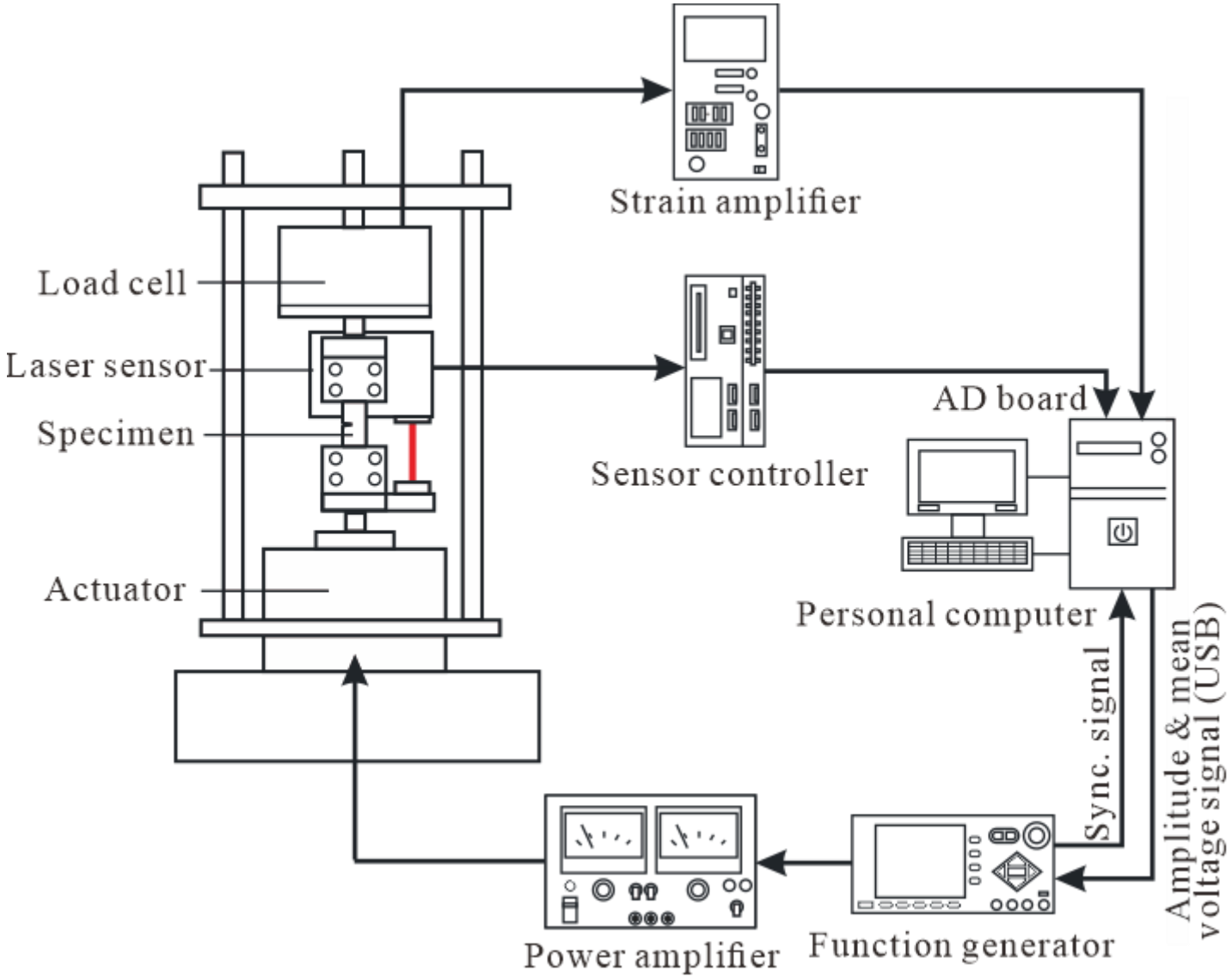

Figure 5. Configuration of fatigue test system.

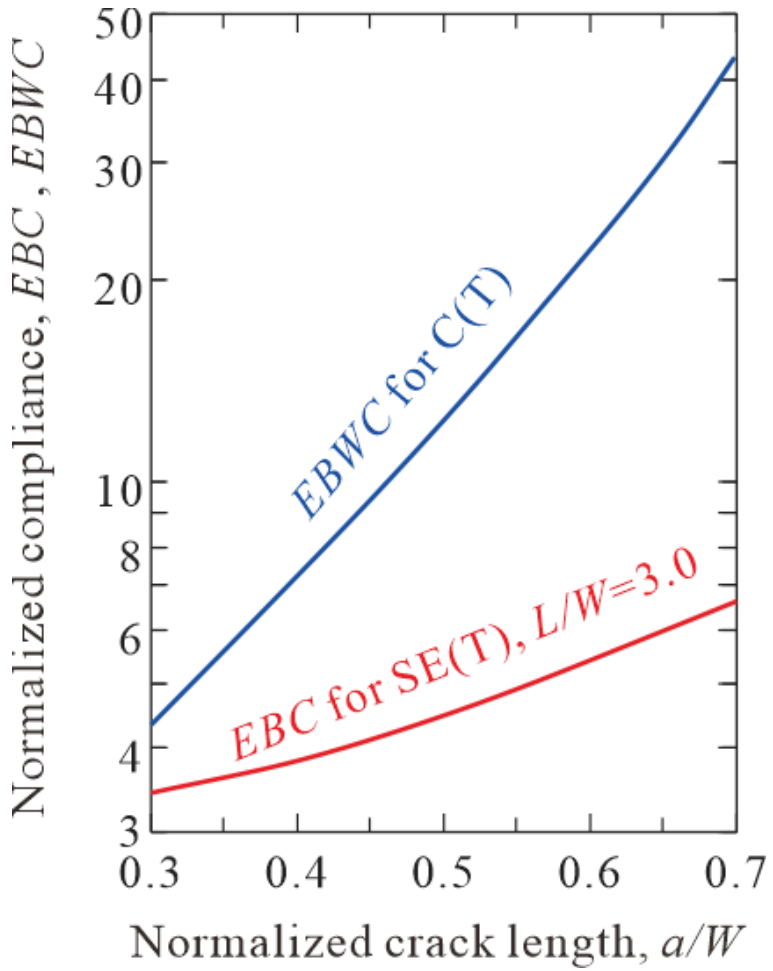

Figure 6. Change of compliance with crack growth, where E: Young's modulus of material, W: width of specimen, B: thickness of specimen, C: compliance, L: gauge length)

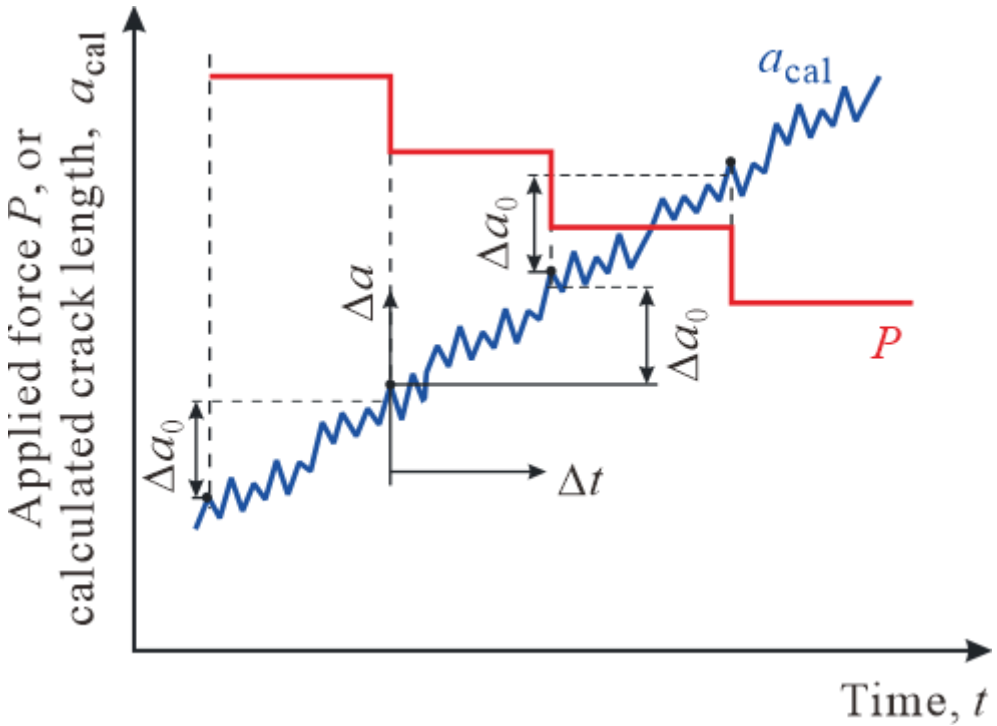

Figure 7. Stepped force shedding procedure.

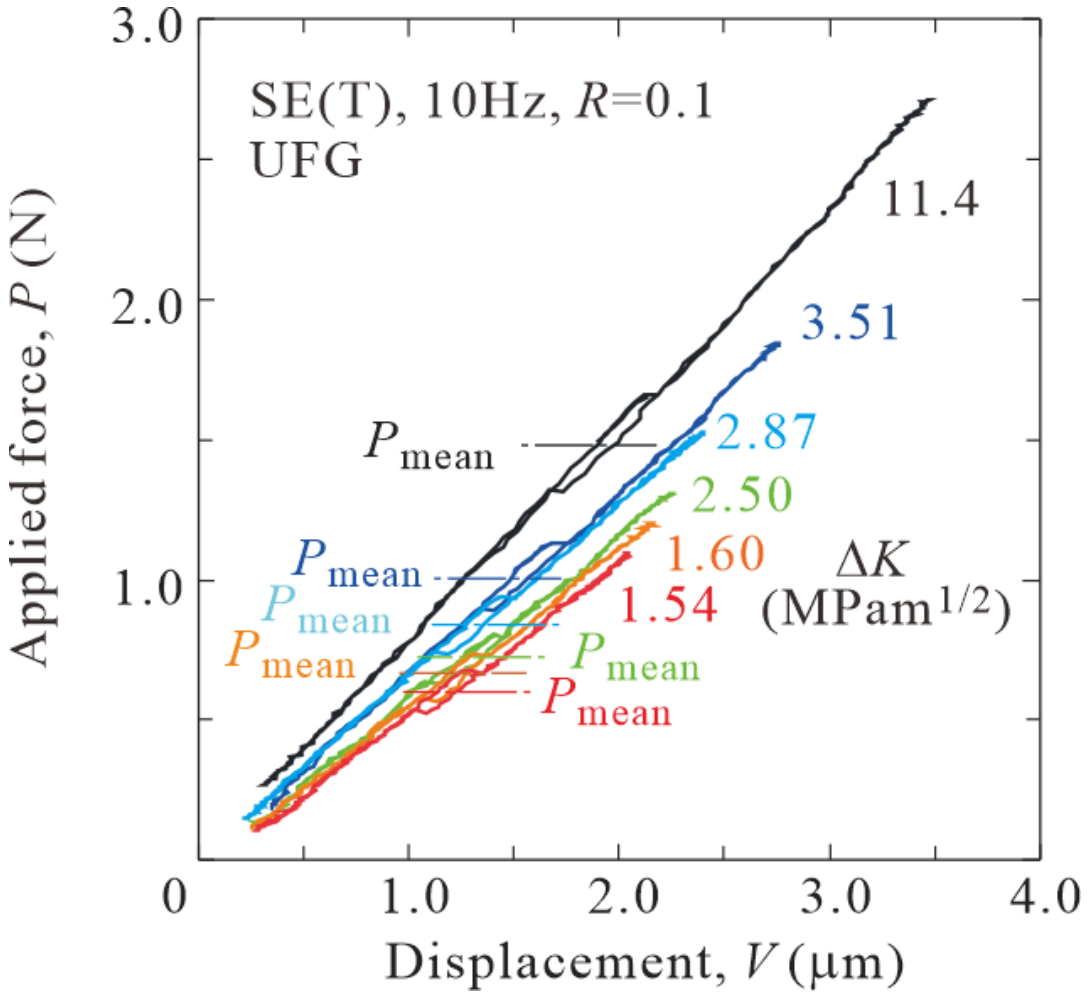

Figure 8. Force–displacement curves obtained from force shedding fatigue test of thin SE(T) specimen.

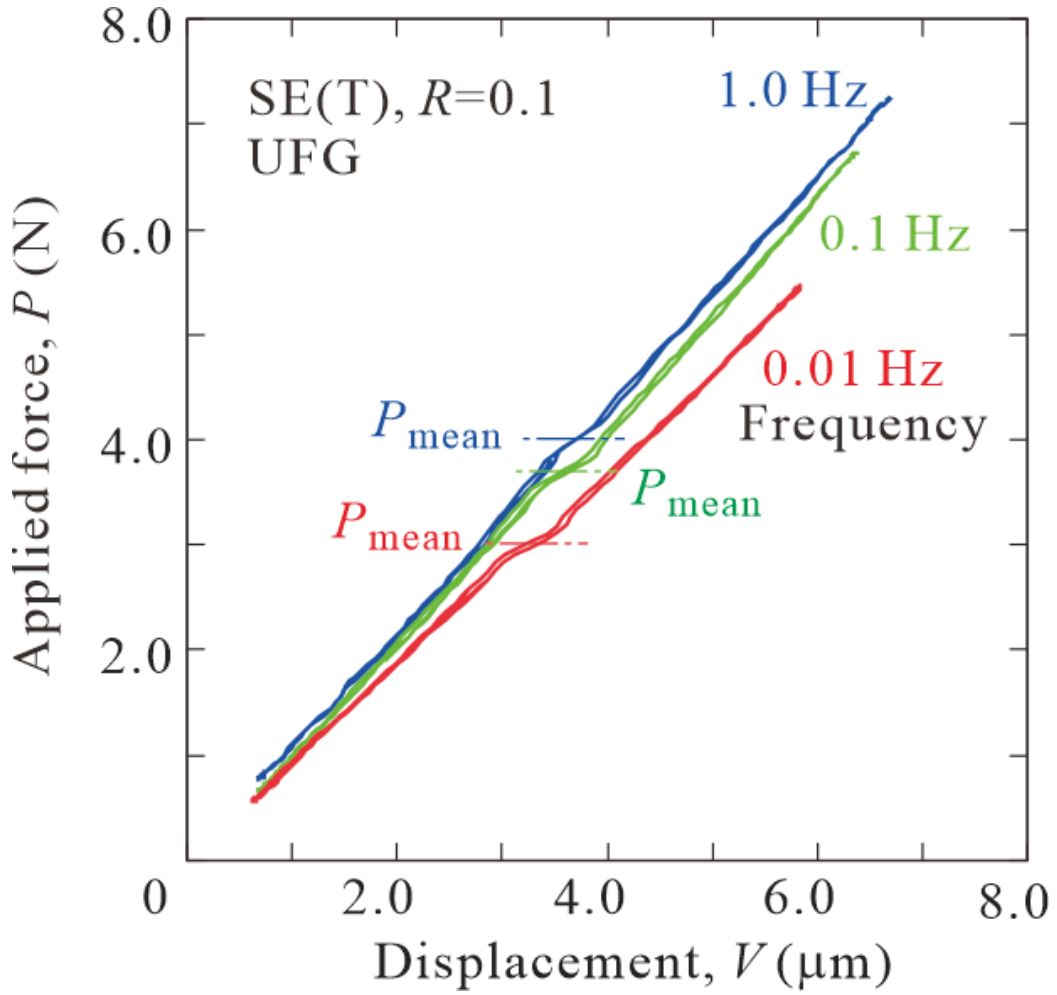

Figure 9. Effect of loading frequency on force–displacement curve for thin SE(T) specimen.

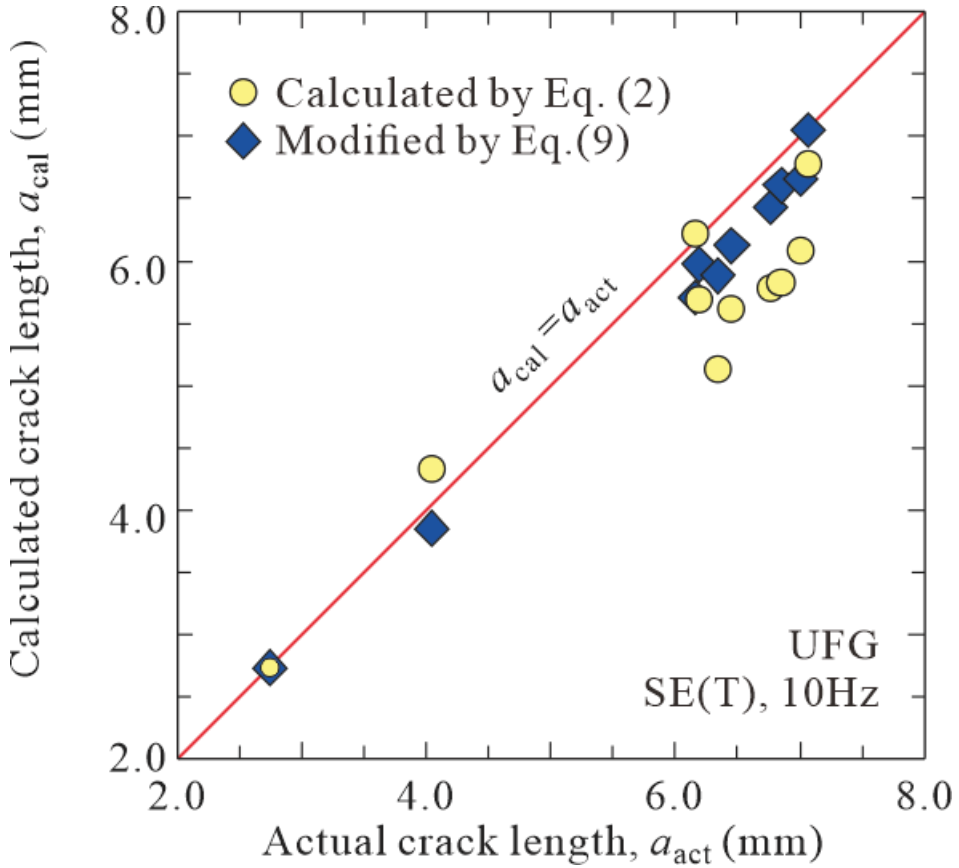

Figure 10. Comparison between measured and calculated crack length for thin SE(T) specimen.

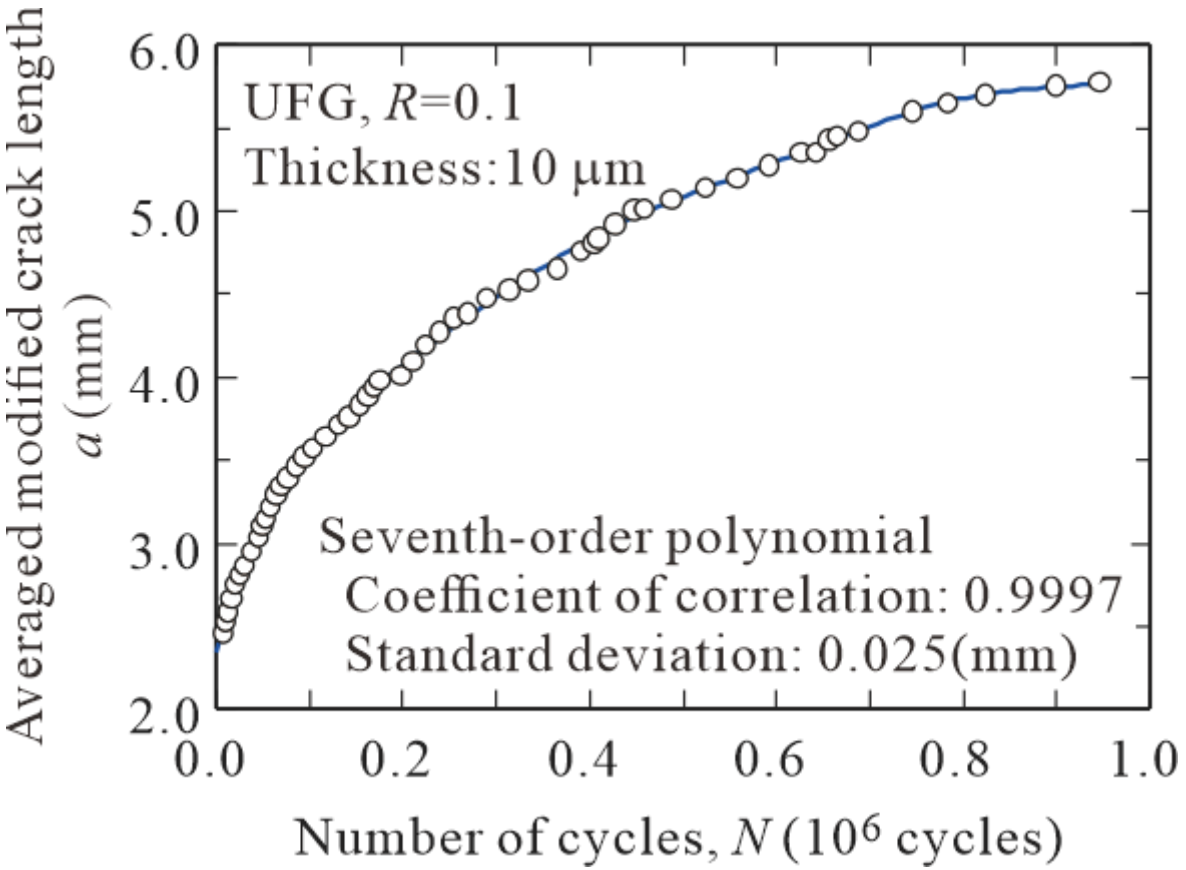

Figure 11. Crack propagation curves for UFG thin film with thickness of 10 μm.

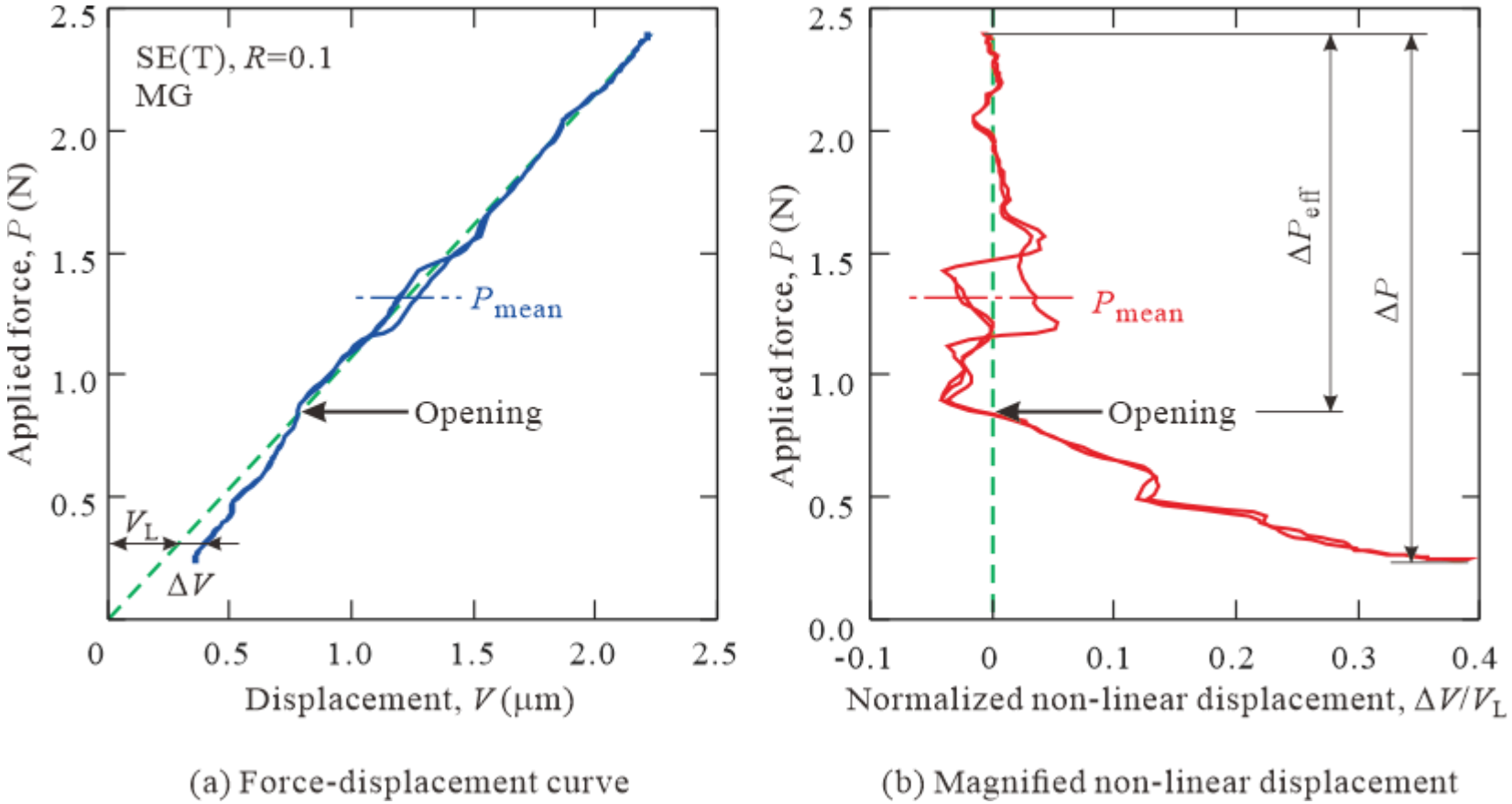

Figure 12. Determination of crack opening force for medium grain size (MG) thin film.

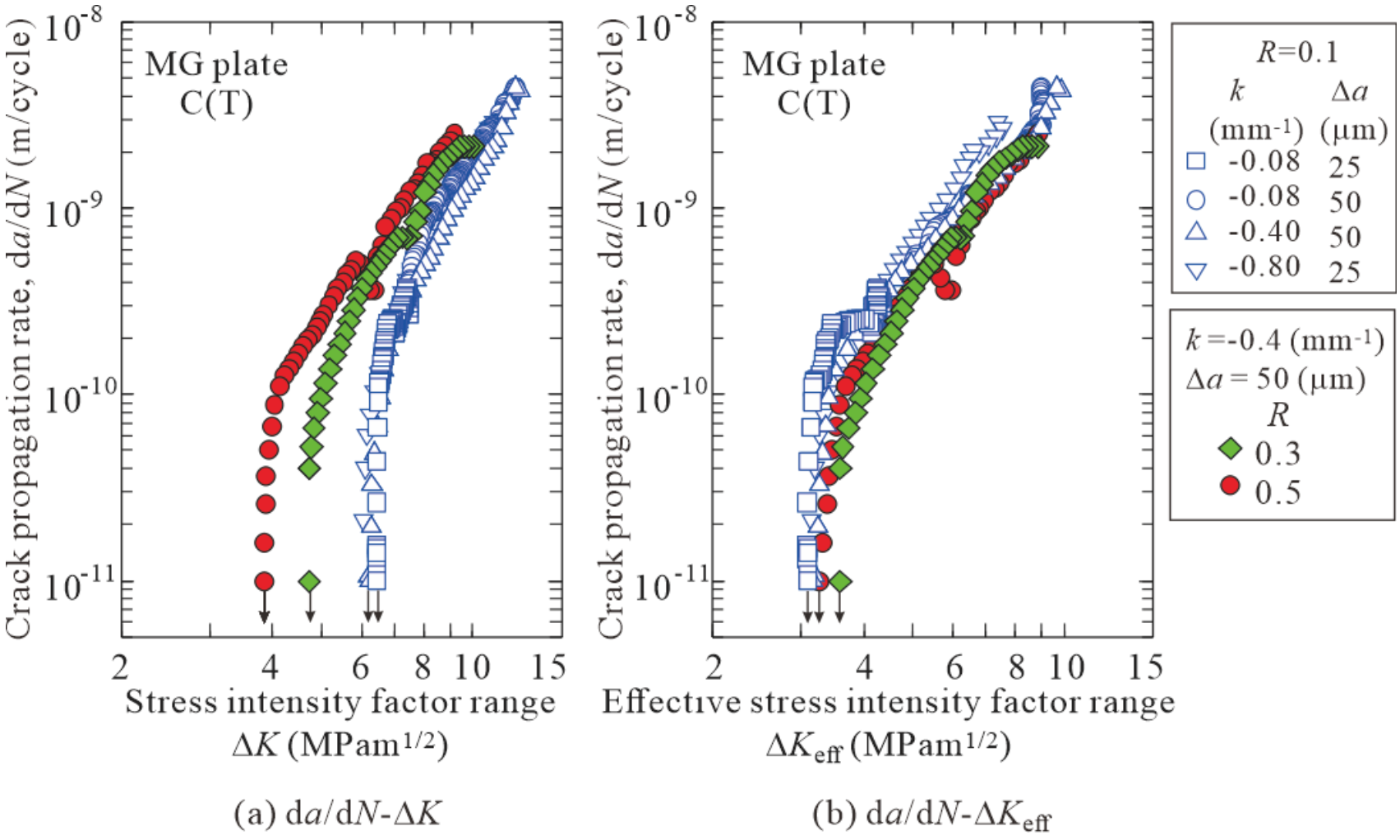

Figure 13. Effect of force ratio on fatigue crack propagation behavior of bulk material.

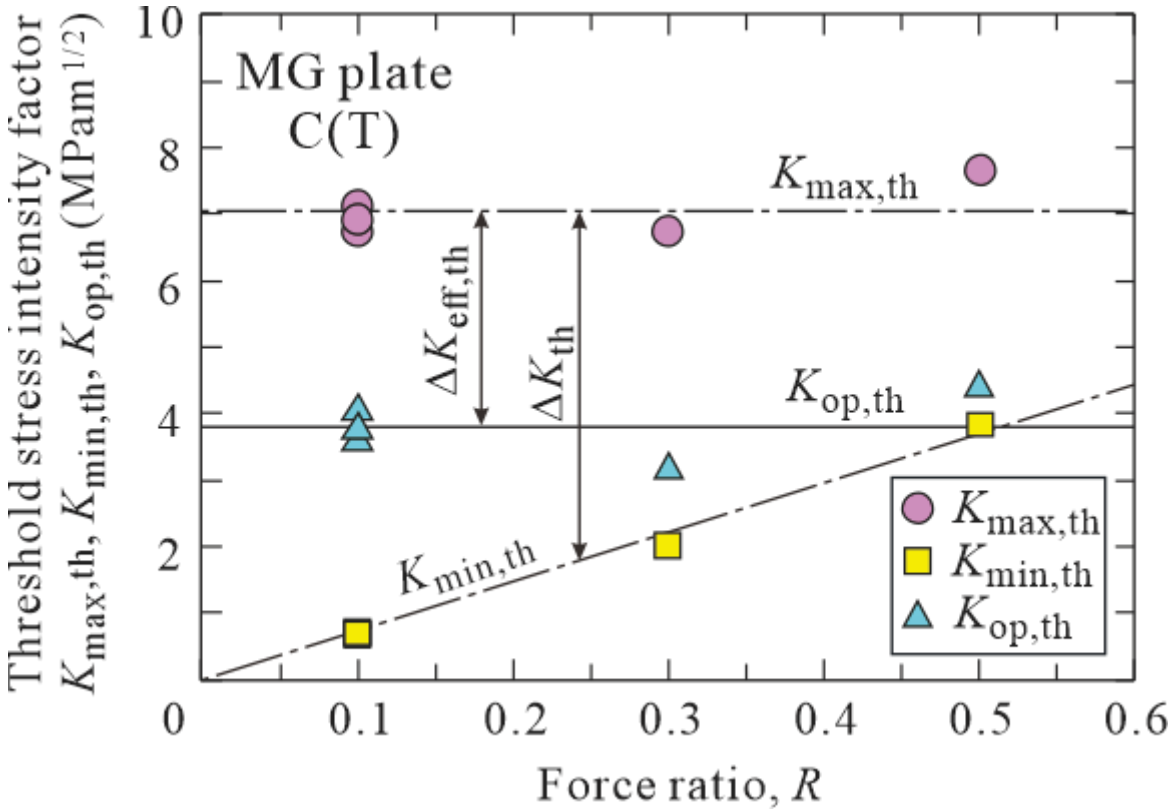

Figure 14. Force ratio dependence of stress intensity factors at threshold condition for bulk material.

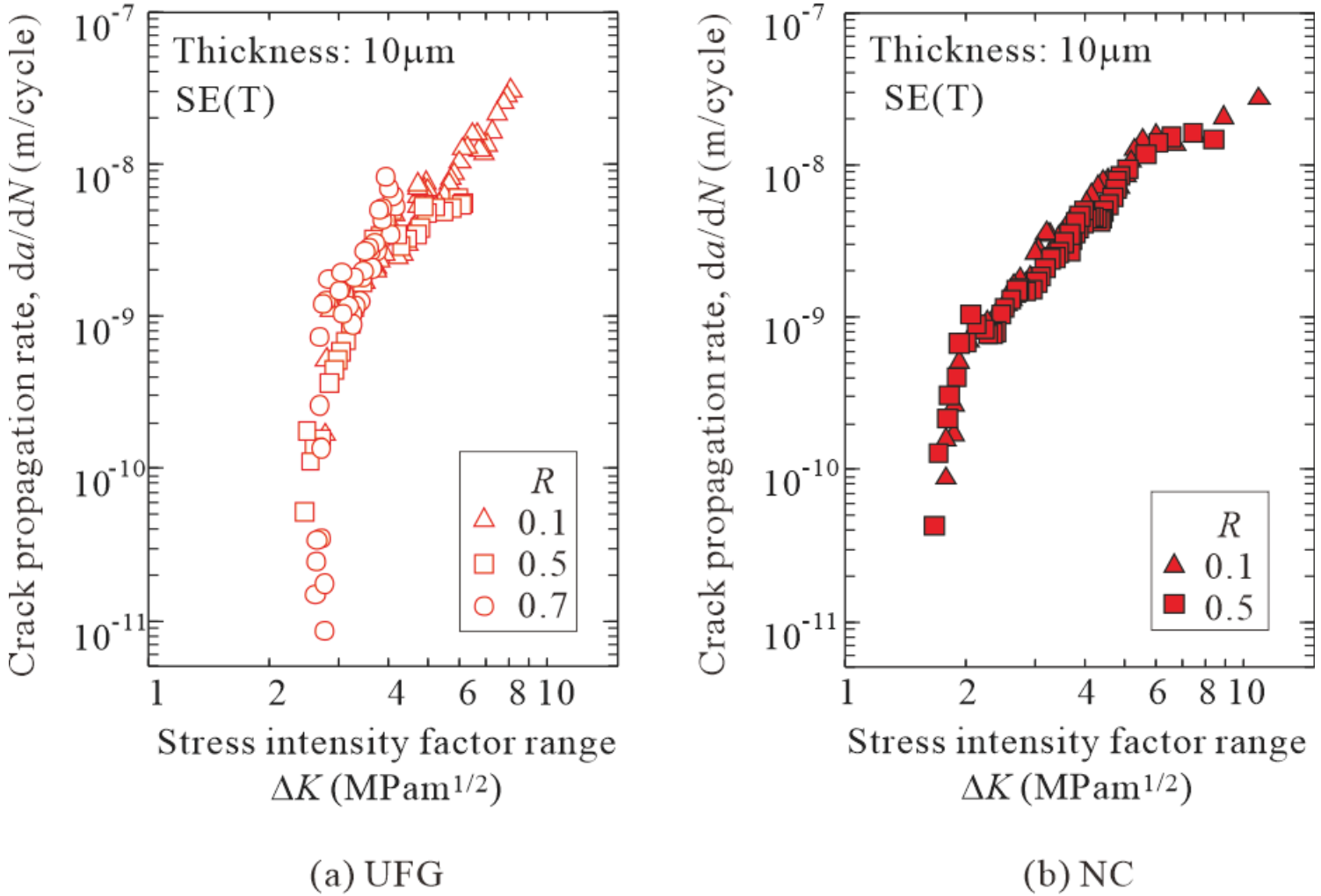

Figure 15. Effect of force ratio on fatigue crack propagation behavior of ultra-fine grained (UFG) and nanocrystalline (NC) electrodeposited thin films of 10 μm thickness.

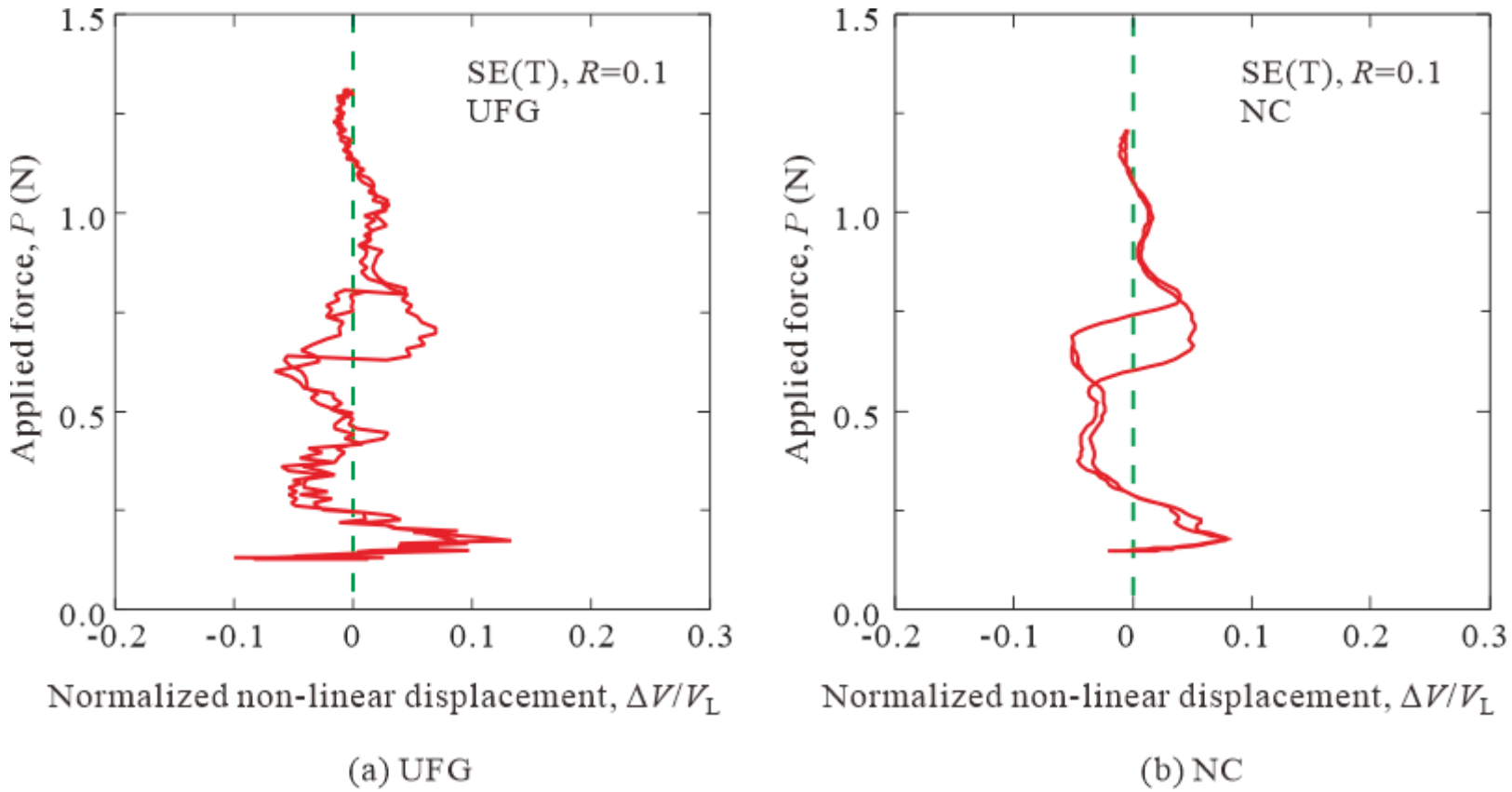

Figure 16. Magnified non-linear displacement as a function of applied force at threshold condition of R = 0.1.

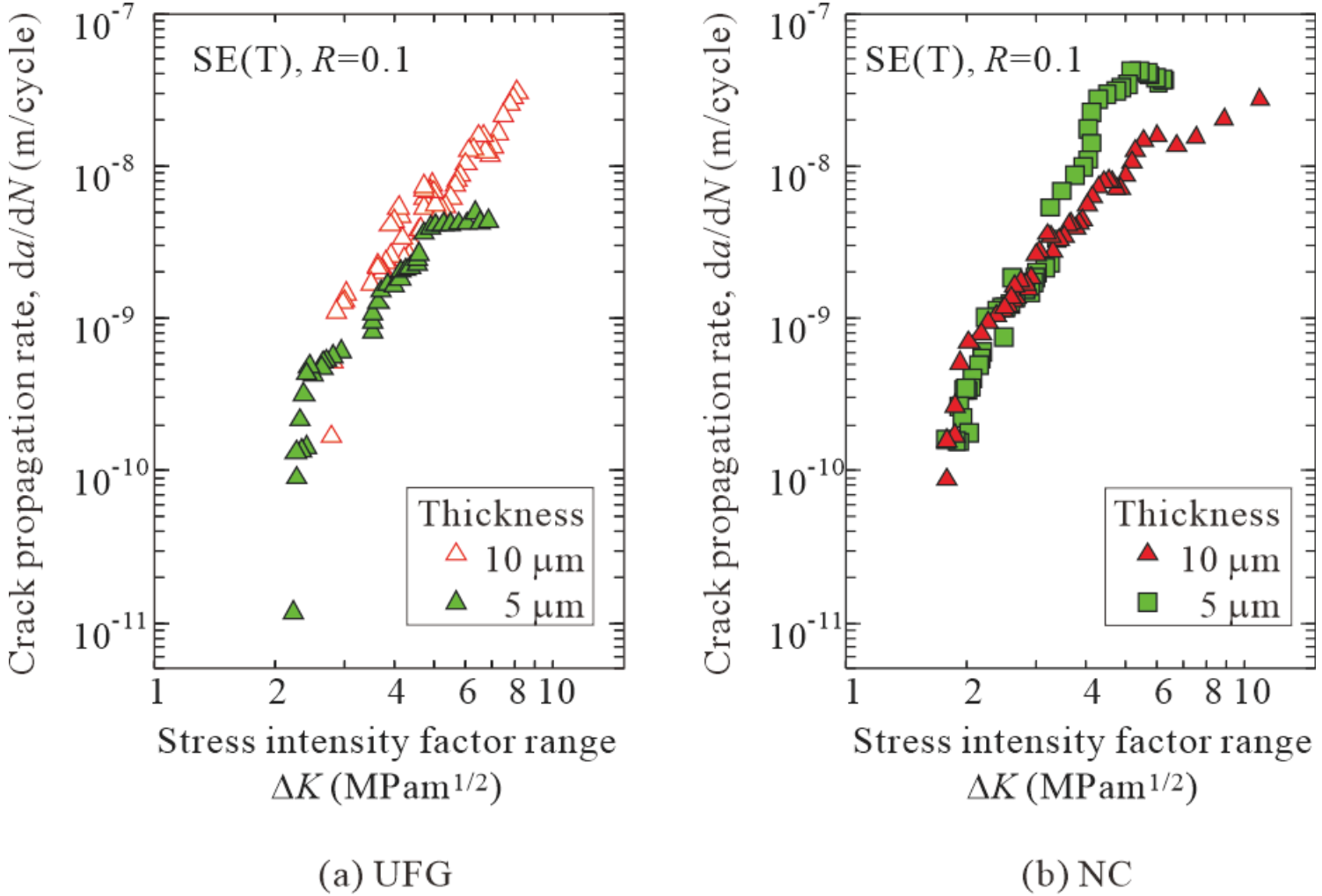

Figure 17. Effect of film thickness on fatigue crack propagation behavior of electrodeposited ultra-fine grained (UFG) and nanocrystalline (NC) thin films.

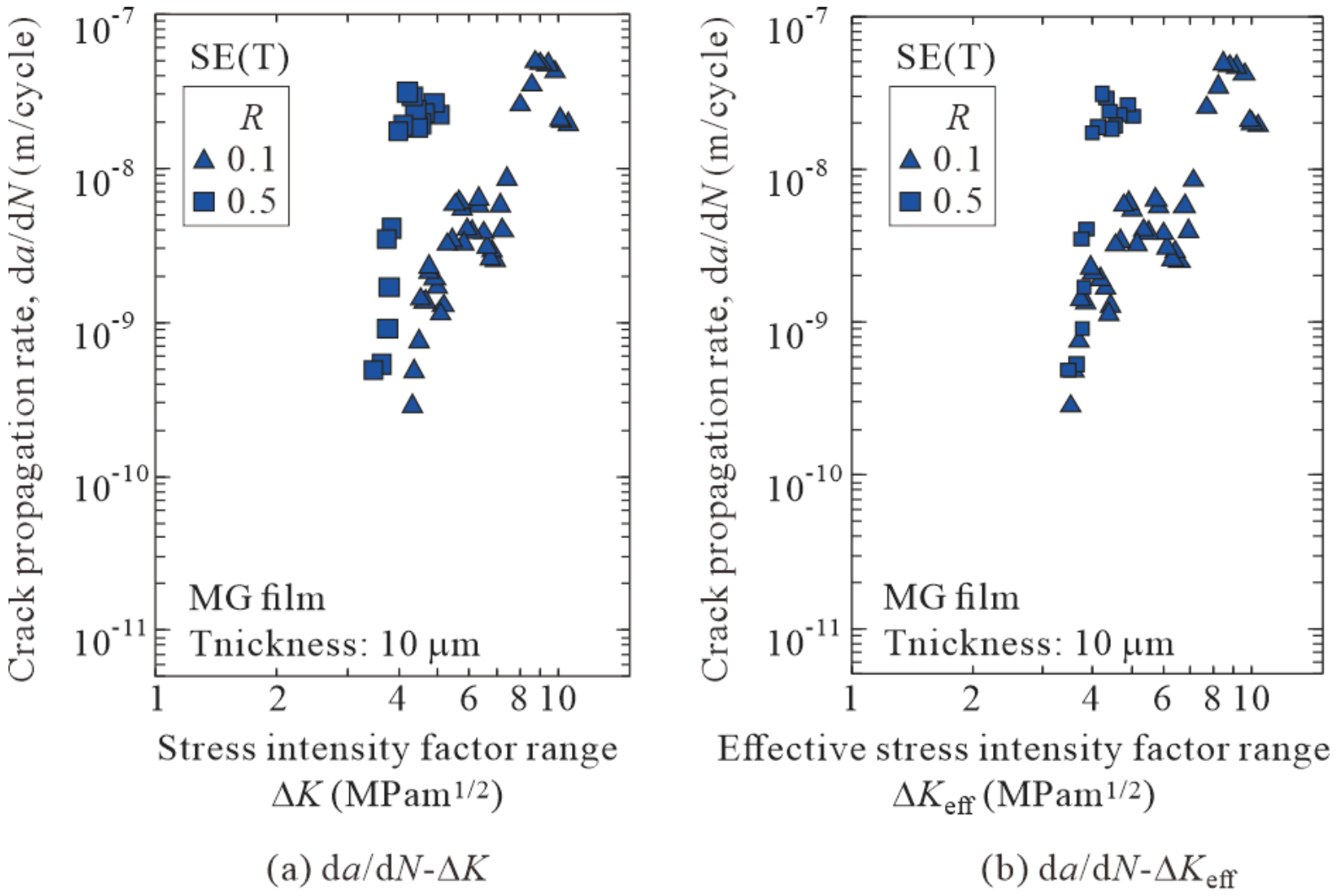

Figure 18. Effect of force ratio on fatigue crack propagation behavior of medium-size-grained (MG) film of 10 μm thickness.

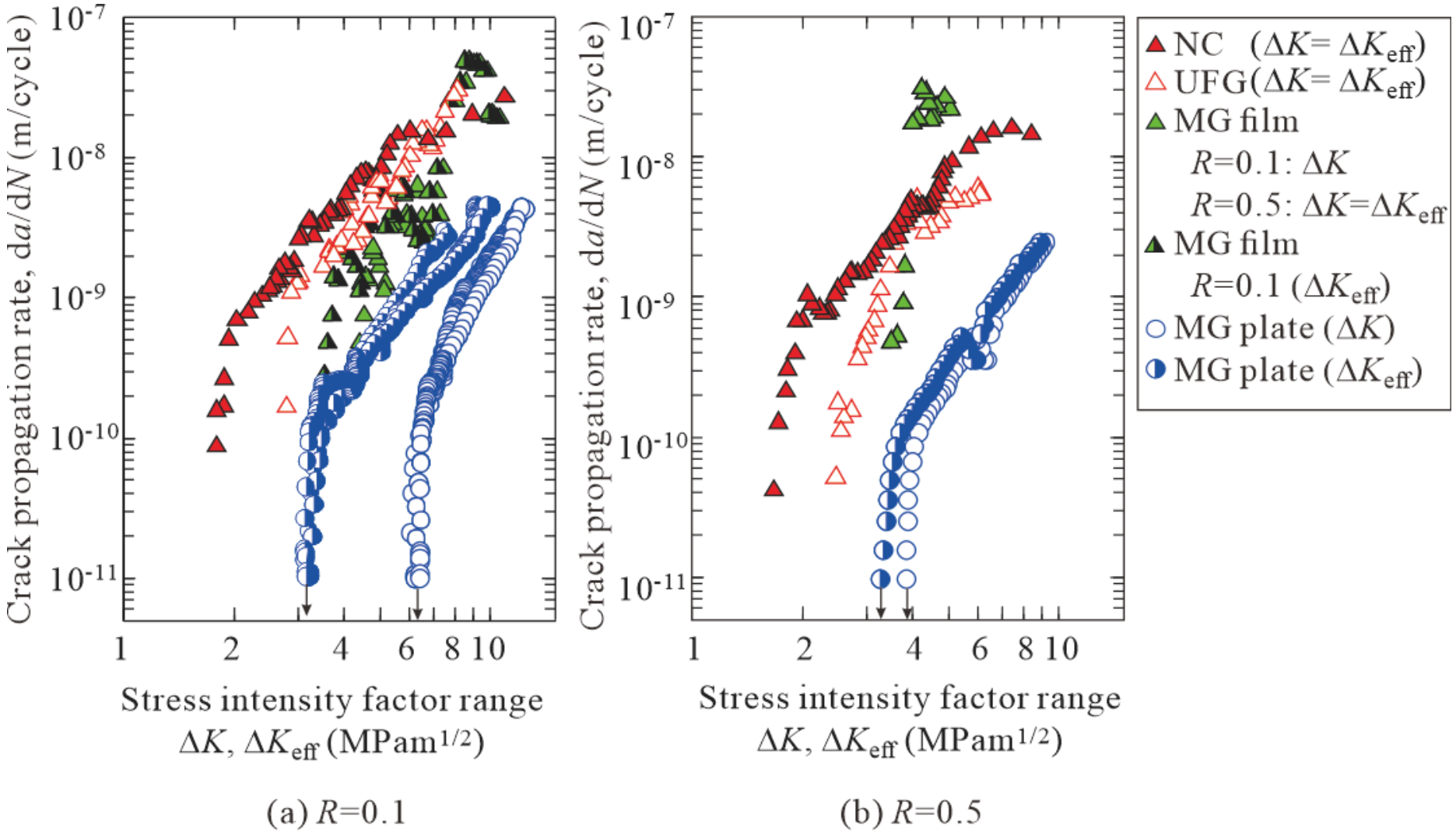

Figure 19. Effect of microstructure and thickness on fatigue crack propagation behavior of pure nickel.

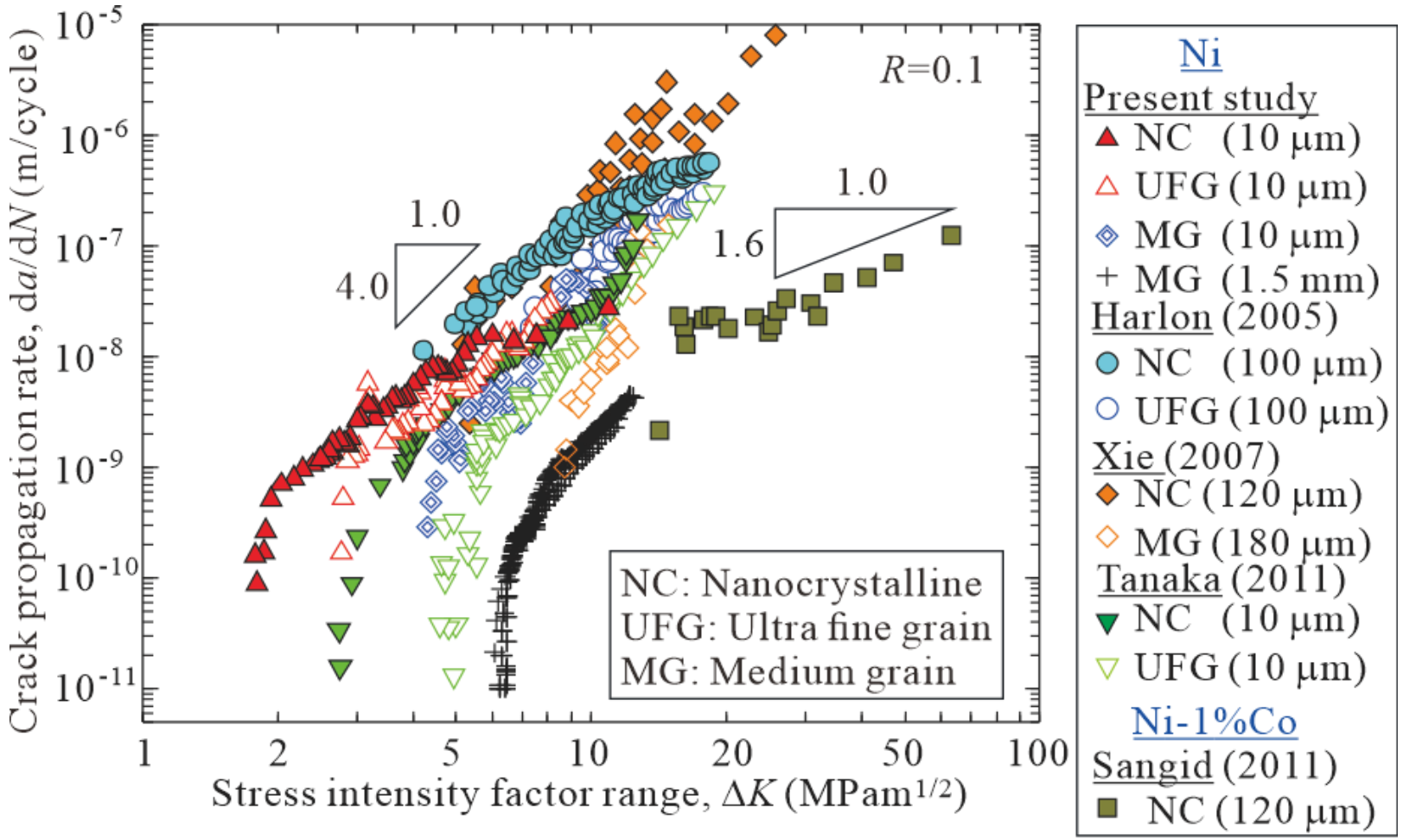

Figure 20. Effect of microstructure and thickness on fatigue crack propagation behavior of electrodeposited nickel film and bulk nickel plate, where the thickness of the thin specimen is 10 μm for the present study and Tanaka et al., 100 μm for Hanlon et al., 120 μm for Sangid et al. and NC of Xie et al., 180 μm for MG of Xie et al., and 1.5 mm for MG plate for the present study

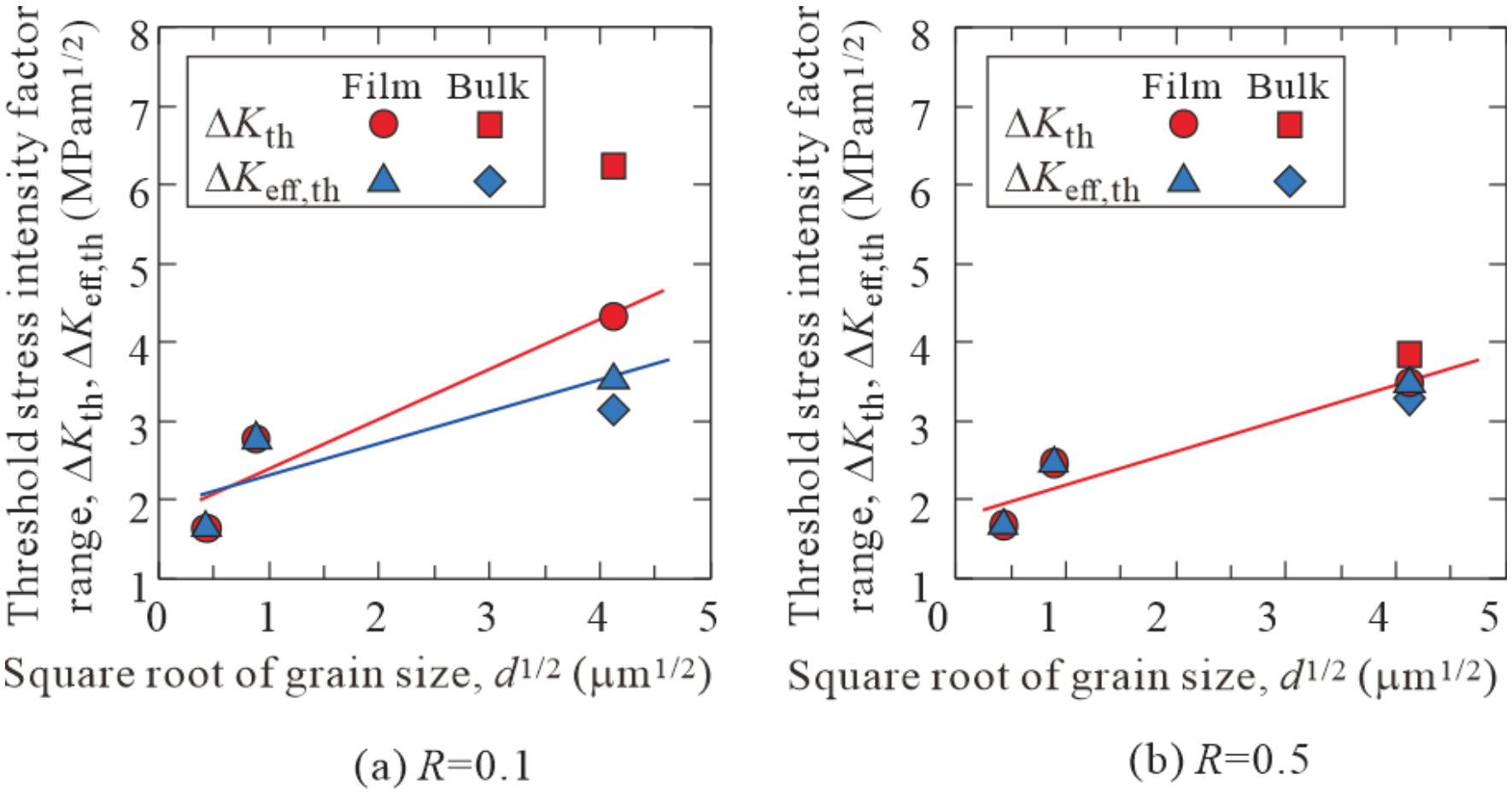

Figure 21. Effect of grain size on fatigue crack propagation threshold.

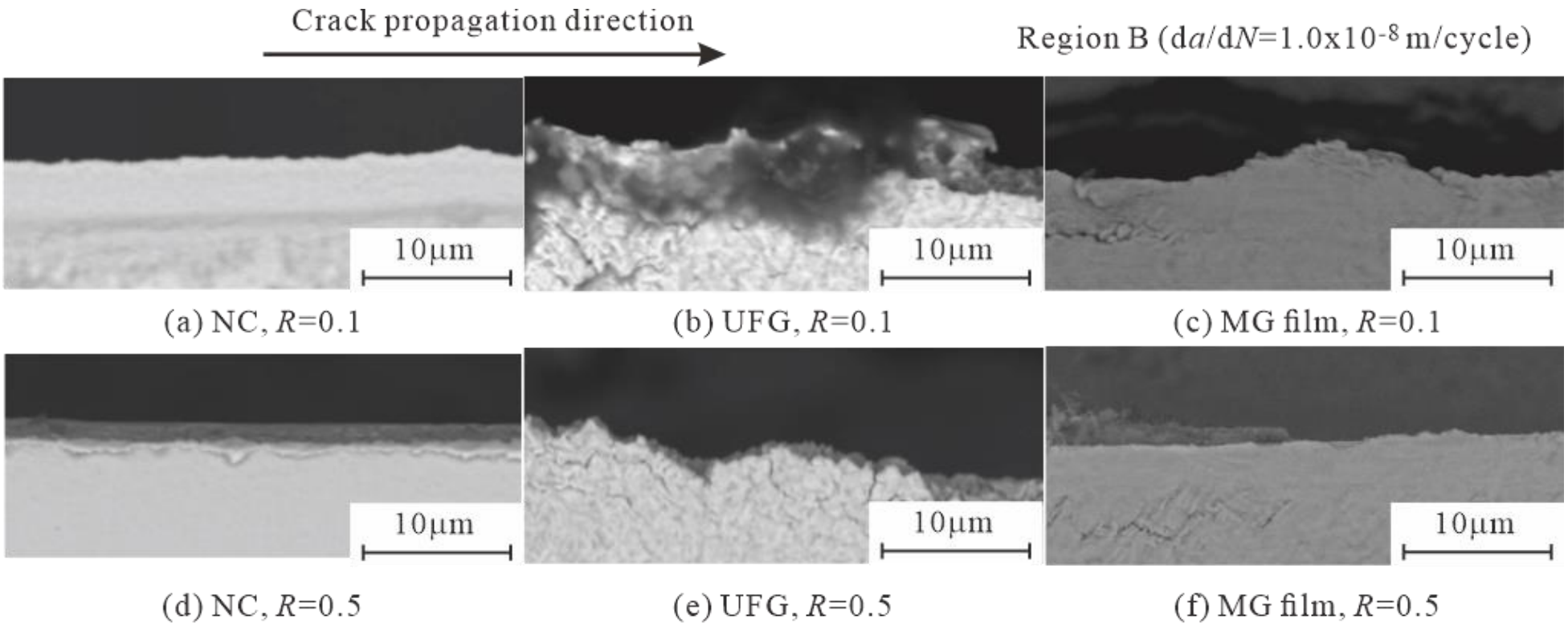

Figure 22. Crack path in Region B (da/dN=1.0×10^{-8} m/cycle) of thin films.

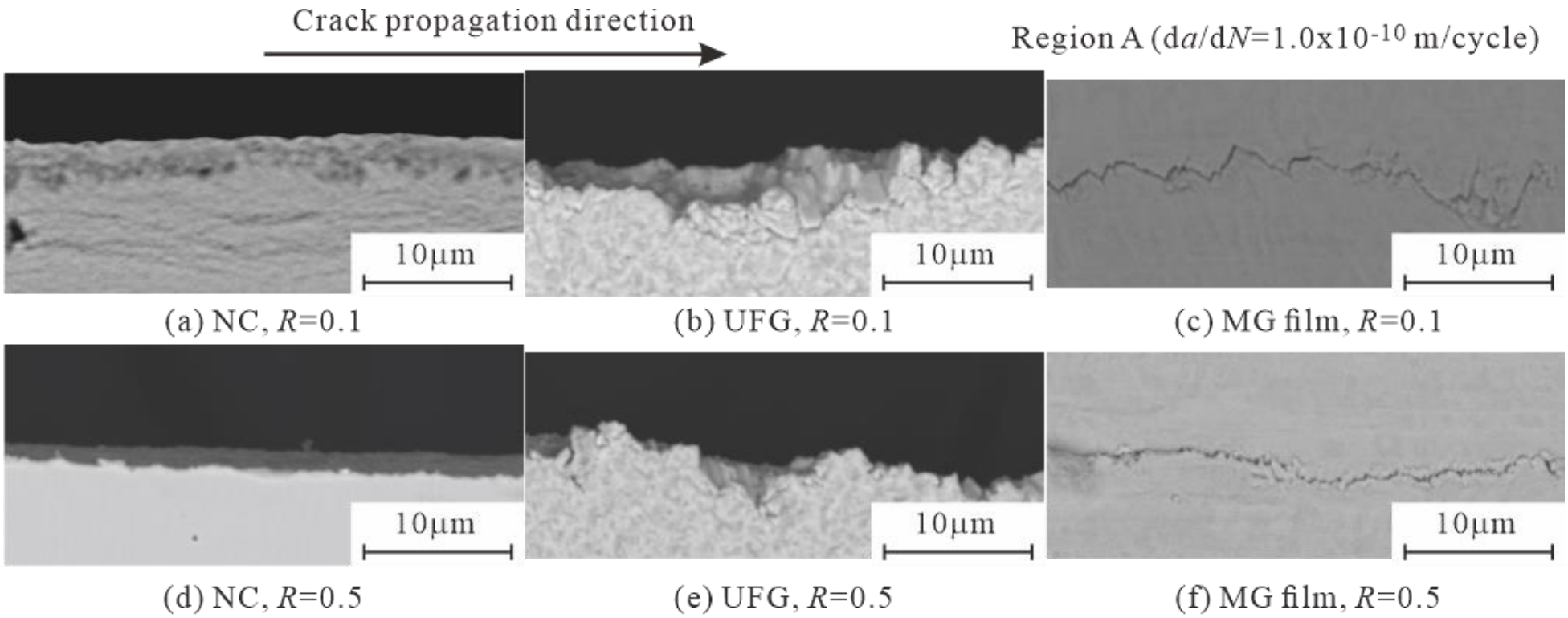

Figure 23. Crack path in Region A (da/dN=1.0×10^{-10} m/cycle) of thin films.

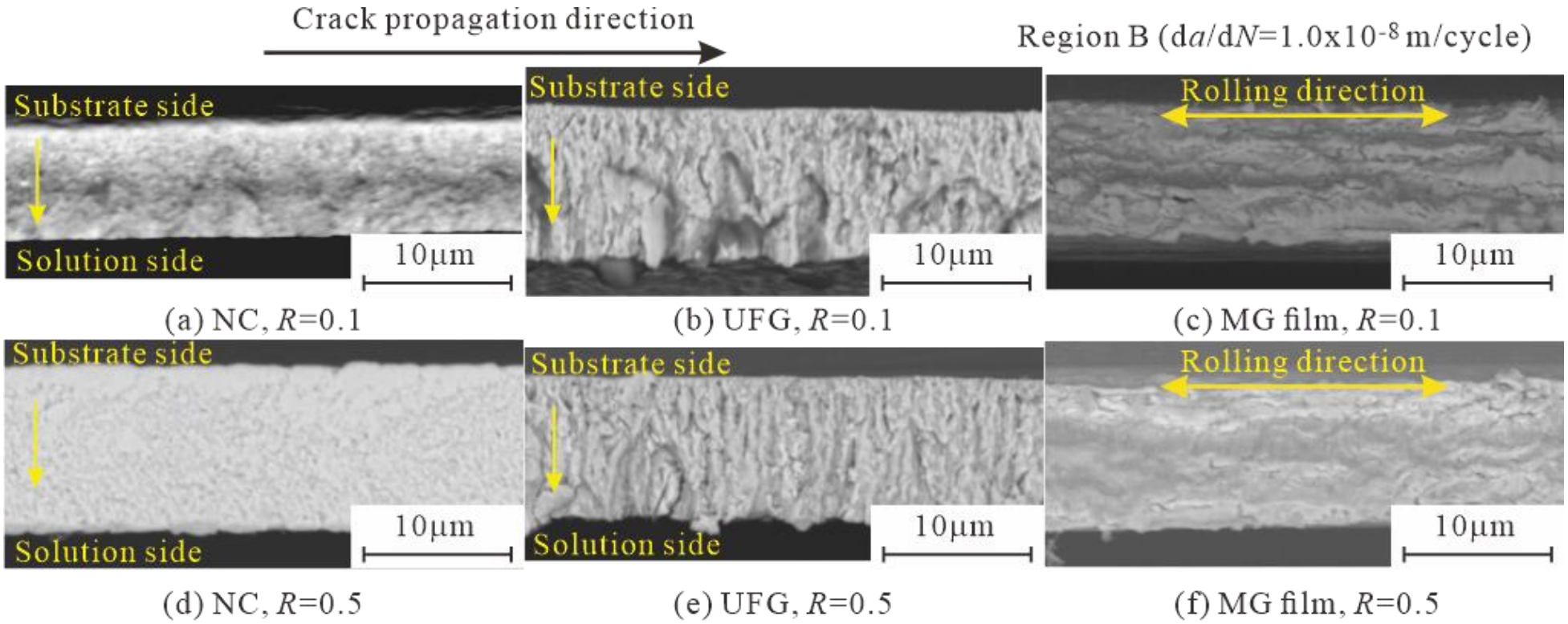

Figure 24. Fracture surface in Region B (da/dN=1.0×10^{-8} m/cycle) of thin films.

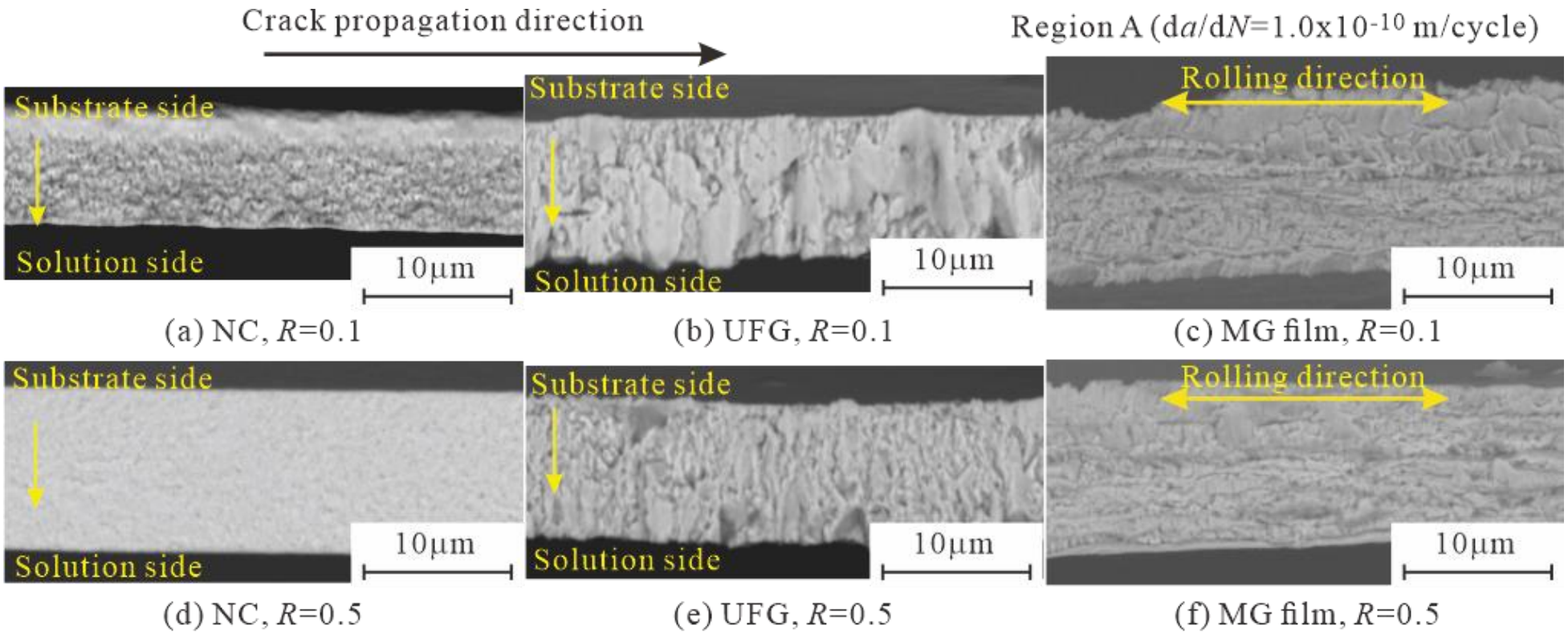

Figure 25. Fracture surface in Region A (da/dN=1.0×10^{-10} m/cycle) of thin films.